Summer 1998

Coupled Electrodynamic-Monte Carlo Simulations of Nanoscale GaAs Terahertz Optical Mixers

Jiang Li
Old Dominion University

Recommended Citation

Li, Jiang. "Coupled Electrodynamic-Monte Carlo Simulations of Nanoscale GaAs Terahertz Optical Mixers" (1998). Master of Science (MS), Thesis, Electrical & Computer Engineering, Old Dominion University, DOI: 10.25777/b42h-tm31
https://digitalcommons.odu.edu/ece_etds/413

Coupled Electrodynamic-Monte Carlo Simulations of Nanoscale GaAs Terahertz Optical Mixers

By

Jing Li
B.E. in Electronic Engineering
Tsinghua University, Beijing, P.R.China

A Thesis Submitted to the Faculty of
Old Dominion University in Partial Fulfillment of the
Requirements for the Degree of

MASTER OF SCIENCE

ELECTRICAL ENGINEERING

with an Emphasis on Physical Electronics

OLD DOMINION UNIVERSITY
AUGUST 1998

Approved by:

Ravindra P. Joshi (Director)

Peter L. Silsbee

Linda L. Vahala

ABSTRACT

COUPLED ELECTRODYNAMIC-MONTE CARLO SIMULATIONS OF NANOSCALE GAAS TERAHERTZ OPTICAL MIXERS.

Jing Li
Old Dominion University, 1998
Director: Dr. Ravindra P. Joshi

The concept of mixing or heterodyning has traditionally been used for microwaves and for radio frequency communications. However, the concept can easily be extended into the optical frequency regime. By doing so, the photomixing process can serve as a very versatile tool for both the generation of ultrahigh frequency (terahertz) and the detection of weak optical signals.

The aim of this thesis is to perform a theoretical study of the photomixing process inside GaAs devices as the non-linear elements. A coupled approach which combines the Monte Carlo simulation scheme for the carrier transport, with Maxwell's equation for the electrodynamics, has been developed. The full wave time-domain computations are necessary to accurately keep track of the electromagnetic fields during the photomixing process. The simple Poisson equation or the frequency domain transfer function approaches become inadequate over the ultra-fast time scales. Besides, the physics of wave propagation, radiative output, and magnetic field effects is ignored by the simpler scheme.

Results for the time dependent photocurrent resulting from the mixing of two laser inputs have been obtained. The conversion efficiency and current magnitude are analyzed as a function of several important parameters: input wavelength, device dimensions, applied bias, and incident power intensity. The simulation compares well with available data and predictions are made in this thesis study for achieving higher efficiency of operation.

Co-Directors of Advisory Committee: Dr. Peter L. Silsbee
Dr. Linda L. Vahala

ACKNOWLEDGEMENTS

I would like to express my sincere appreciation to my advisor Dr. Ravindra P. Joshi for his guidance, ideas and support throughout this research project. His help, patience and friendship made this thesis possible. It is a great honor and pleasure to work with him. I also wish to thank Dr. Peter L. Silsbee and Dr. Linda L. Vahala for serving on my thesis advisory committee.

I am very thankful to my family for their support and belief in my ability. They provide me a constant source of love and encouragement while I pursued my education.

I must acknowledge the valuable help and assistance from my friends Qiong Chen, Lifeng Zheng, Zhicheng Lai, Wenhui Shi, and Lan Luo.

TABLE OF CONTENTS

LIST OF TABLES

LIST OF FIGURES

CHAPTER I

INTRODUCTION

1.1 Optical Heterodyning

In many applications it becomes necessary to combine two or more signals and generate an output consisting of a multitude of waveforms and their harmonics. These output waveforms are usually available at the sum and difference frequencies. Such an output can be generated provided the mixing element used to combine the input signals has non-linear response characteristics. The overall process of mixing, in effect, redistributes the energy from an input set of frequencies to a different (and usually larger) set of output frequencies. Though the output signals are usually not as strong, the advantage of this "heterodyning" or mixing process is the availability of signals at much lower frequencies due to the "down-conversion" process. It is usually desirable to obtain signals at the lower frequencies, since the frequency response of electronic circuits is much better. As a result, it becomes far easier to amplify and electronically process the lower frequency output than the original input signal. Thus, heterodyning can be used to take advantage of the detection and amplification of weak, high frequency signals.

In addition to their role in detectors, mixing input signals can also be a very useful means of generating output radiation at a desired sum or difference frequency. In such a case, the mixing would typically be used to "up-convert" and produce a coherent source of high frequency radiation. The coherence is an important aspect, since it can allow for the delivery of high power densities. In principle, any desired output frequency can be generated.

The concept of mixing or heterodyning has traditionally been used in the context of microwaves and for radio frequency communications. Schottky diodes have been used as the non-linear mixing elements because of their fast response and reliability. Many treatments of such radio frequency mixing and semiconductor mixer systems are available [1-3]. However, the concept of heterodyning can easily be extended into the optical frequency range as well. By doing so, the photomixing process can serve as a very versatile tool for both the generation of ultra-high Terahertz (THz) frequencies and the detection of weak optical signals. Delectability is almost impossible to achieve in the THz range due to the limited frequency response of electronic circuits. Signal generation at the much lower microwave frequencies can currently be achieved by solid state coherent sources or three-wave-mixing techniques in non-linear crystals. However, beyond the Gigahertz range, the solid state sources provide neither good frequency tunability nor efficient operation, while the three-wave mixing strategies require very stringent phase matching. In view of the disadvantages mentioned above, the optical heterodyne technique appears to have advantages and is now beginning to attract considerable interest.

However, optical heterodyning was not an important viable technique for a long time. This is due to the lack of high-quality optical sources and the absence of high quality reproducible device structures. Furthermore, the output power range of optical mixers tended to be below the microwatt range [4]. This limited their utility.

Fortunately, the development of new stable and rugged tunable lasers, and the advances in high-speed III-V device technology have changed the future of optical heterodyning. The lasers provide for precision coherent optical signals. These signals can be used as stabilized inputs to drive optical mixer elements for the generation of high frequency coherent optical radiation. In addition, these lasers can often function as the means of efficient detection based on absorption and transmission spectroscopy (ATS). However, such ATS signals tend to be weak in intensity and their direct detection is not very easy. In this regard, the optical mixing concept can be very useful for monitoring such weak laser signals. For instance, the weak laser ATS signal could be mixed with that from a strong local oscillator and fed into an optical heterodyne system. The output would then contain all the characteristics and details of the weak ATS signal at a down-converted frequency.

The development of high-speed III-V technology is also important from the standpoint of fabricating reliable photomixing elements. GaAs technology has been used as the medium for combining the optical signals. For good response at high frequencies, it is necessary to have high-speed material that can withstand continuous operation. The direct bandgap GaAs material with its high electron mobility, and non-linear electrical response characteristics, is likely to be an ideal candidate. Several efforts at optical mixing in the THz frequency range have begun to emerge. Many experiments on this concept have shown that the output frequencies in the THz range could be achieved successfully [5-8].

1.2 Photomixing Scheme and Related Issues

The research work in this thesis is mainly driven by a need at the National Aeronautics and Space Administration (NASA) to detect weak optical signals. These optical signals arise in connection with atmospheric remote sensing applications. The sensing method relies on the absorption and transmission measurements of laser beams.

The laser beams propagate through the atmosphere, and are used to detect various gaseous species and their densities based on ATS. In general, the optical laser signals received could be modulated in intensity (due to atmospheric fluctuations) and could be quite weak in strength. Direct detection is therefore not very easy, and is further complicated by the background noise that is often associated with such atmospheric signals. Optical heterodyning is being proposed as a possible detection scheme. The basic concept involves the following:

(i) The generation of high power optical beams from local oscillators (LO). The frequency of the local oscillator optical signal would deliberately be kept very close to that of the optical signal to be detected. For convenience and simplicity, stabilized lasers would be used both for the LO source and for the optical signal for atmospheric sensing. For better performance, the LO source and the atmospheric signal could be the adjacent modes of a cw laser. Hence, their frequencies would be ω_1 and ω_2, with $\omega_1 \cong \omega_2$. The development of stabilized lasers operating at nearly identical frequencies with close phase matching is thus central to the success of the overall scheme. Fortunately, such laser systems have been set up at NASA.

(ii) Both the LO and the weak atmospheric signal to be detected can then be focused on a GaAs optical detector. This semiconductor medium would serve as the non-linear photomixing element. A suitable voltage bias applied to the GaAs would create an internal field. Absorption of both the incoming LO and the atmospheric optical signals would then generate photocurrents within the GaAs material in the presence of the applied bias. Since the photogeneration process depends on the incoming power intensity, the photocurrent would naturally be modulated at the optical signal frequencies and by any amplitude variation that might be present in the atmospheric signal. The former gives rise to sum and difference frequency variations.

(iii) High frequency photocurrents at the sum frequencies and their harmonics would essentially average out to a zero value and have no significant role. However, variations at the lower difference frequency would give rise to a modulated photocurrent with a non-zero dc value that could be detected. The presence of a strong local oscillator signal would automatically give rise to a substantial photocurrent even if the atmospheric optical signal were weak.

(iv) In principle, the photocurrent variations containing modulations of the atmospheric signal could be detected directly through electronic amplifying circuits. However, the difference frequency $|\omega_1 - \omega_2|$ is still in the terahertz range, and well beyond the scope of conventional electronic circuits. A possible scheme being proposed for overcoming this poor frequency response of electronic detection systems is to use the mixer photocurrents to drive an antenna structure. The photocurrents fed into a suitable impedance matched antenna would produce radiation. Such radiation could be easily detected by bolometers and receiving antennas. Furthermore, the intensity modulations of such detected radiation would directly depend on variations of the incoming atmospheric signal. Thus, in this manner, characteristics of the weak incoming atmospheric signal could be obtained via the intermediate optical photomixing process.

The overall problem of weak optical signal detection is complex, and requires the development of all the related hardware. Besides coherent precision lasers, suitable GaAs photomixing devices have to be fabricated. The GaAs material parameters and device dimensions have to be optimally chosen for maximum optical mixing and photocurrent generation. This in itself is an open question and challenging task. Since this concept is relatively new, not much work has been done in the literature on the optimized GaAs design. Next, there are unresolved issues concerning the type of antennas to be used for radiating the mixed photocurrent signals. The choice of the line impedance and the close matching between their values and the antenna load structure for maximum power throughput are also an important task. Finally, aspects related to the optical focusing of radiated signals towards the bolometers and receiving antennas also merit attention.

1.3 Overview of Thesis Research Objectives

As outlined above, the overall problem of developing and optimizing the performance of a terahertz photomixer is very challenging and fairly broad in scope. This thesis research will focus on a small portion of the problem relating to the theoretical evaluation and performance predictions of the GaAs photomixer. Thus, aspects regarding the generation and focussing of laser signals onto the GaAs material, details of the microwave circuits for feeding the photocurrents through antenna structures, and the subsequent radiation and detection by bolometers will not be addressed in this thesis. The numerical modeling of the GaAs photomixer medium and its response would serve the following objectives:

(i) Theoretical testing and validation of the photomixing concept.

(ii) Predictions of the photocurrent response and its time-dependent behavior at the terahertz input frequencies. Simulations at such high frequencies have not been carried out to the best of our knowledge.

(iii) Quantitative predictions on the effectiveness of the photomixing which is a non-linear process. The output power levels and conversion efficiencies at the terahertz frequencies would also be provided. Where ever suitable comparisons with available experimental data will be made.

(iv) Evaluation of the photocurrent response on several input parameters for optimizing the device output. These parameters include input laser wavelengths, photon flux, photomixer biasing, device dimensions, GaAs material properties and operating temperature. Such optimization can best be carried out through numerical simulations, since a large parameter space can be probed without any costly fabrication.

(v) Providing quantitative trends with variations in the operating parameters, and a best case of photomixer structure, which could then be fabricated, characterized and tested.

In particular, the thesis work on photomixing will mainly concentrate on low-temperature-grown (LTG) GaAs based devices. The performance of LTG material versus ordinary GaAs will also be probed. Current research findings appear to indicate that LTG material should have remarkable photoconductive properties such as ultra-short recombination time, high breakdown dc field, resistivity and photocarrier mobility [9-11]. As a result of the high breakdown dc field, the generated photocarriers are expected to undergo much higher acceleration inside the device. This should then help increase the radiative power accordingly. The high resistivity is expected to minimize the dark current. Finally, the short recombination time should increase the response of photocarriers and produce stronger output at the high frequencies. However, the shorter recombination times are expected to increase the power dissipation and internal device heating, and may lower the conversion efficiency. Hence, this issue of LTG GaAs needs to be carefully evaluated.

Up until the present, most of the research work on optical heterodyning has been carried out on GaAs based devices with feature lengths in the micron range [12]. However, by reducing the feature size down to the nanoscale dimensions, one can expect much better performance. At these lower dimensions, the carrier transit times would be shorter, the capacitance values lower, and the internal electric fields higher giving rise to faster carrier motion. However, the fabrication of nanoscale devices is much more difficult and expensive than that in the micron range because of the greater precision and smaller tolerances. Hence, it is greatly beneficial to perform simulations for determining the possible benefits and advantages on this type of small devices before costly fabrication. The calculation to be carried out on smaller devices for their performance evaluation, is a step in this direction.

The aim of this thesis is to perform a theoretical study of the photomixing process inside the GaAs devices for both LTG and non-LTG material using Monte-Carlo (MC) simulations. The MC method has been chosen since it can very accurately model the transport processes. A full wave Maxwell equation method will be coupled to the MC procedure to accurately keep track of the electromagnetic fields and their evolution inside the device during the photomixing process. There are two main reasons for the need to include Maxwell equations: (I) Particle motion, and hence the photocurrent is controlled by the driving electromagnetic fields present inside the device. It is therefore critical to evaluate this driving electromagnetic field precisely. (II) Also, the focus of the present simulations is on the terahertz regime. At these ultra-fast time scales, the standard Poisson equation is inadequate to describe the high frequency variations.

Chapter 2 provides a literature review of the research work done in this field. Some experimental results and simulation data are described and discussed to an extent in this chapter. In chapter 3, details of the numerical simulation scheme used in this thesis are presented. The principles of the Monte Carlo method used here for the transport calculations in GaAs semiconductor are explained. The Full Maxwell equations are also introduced, which will be used to accurately update the electromagnetic fields. The discretization procedure and numerical implementation are discussed. Some preliminary results validating the numerical approaches are also given in this chapter. Chapter 4 gives the main results for various sets of simulation cases, and provides the discussions. Both the static field cases and the predictions of a full dynamic calculation are presented. In chapter 5, a summary of simulation results is given followed by some future research goals in this area.

CHAPTER II

LITERATURE REVIEW

2.1 Introduction

This chapter is a literature survey of previous research work related to heterodyne detection, the experimental progress made, and the simulation efforts. We will discuss the development of semiconductor optical heterodyne devices and summarize the progresses in this field for the past few decades. A brief theory discussion on the heterodyne phenomenon is provided first. This is followed by the available experimental results and published data on different photoheterodyne devices. Based on these results, the influence of various parameters on the performance of these devices, and their relative importance, are discussed. Some details on the modeling and simulation aspects are then presented. While reviewing the simulation status, the discussion brings out details regarding the various approximations currently being made. Understanding such approximations is an important step for developing better and more accurate simulators.

2.2 Heterodyne detection

Generally, photodetectors are only responsive to photon flux. This means that the device is insensitive to the optical phase, and it cannot process any phase related information. Fortunately, a new technique called "optical heterodyning", or "photomixing", (also called "light beating") is available. This technique allows for measurements of both the magnitude and phase of optical signals.

The idea of this "optical heterodyning" is equivalent to the idea of "superheterodyne radio receivers". Figure 2.1 shows typical optical heterodyning devices

[13]. According to this plot, the input optical signal is mixed with a coherent reference optical signal called the "local oscillator". These two optical fields superimpose spatially within the photodetector and interfere with each other. This basically means that the electric fields of the two individual optical beams mix, producing a net field that is modulated at the difference frequency. This net field then produces an oscillating current that can be detected later. The detected signal thus carries information about both the amplitude and phase of the signal field.

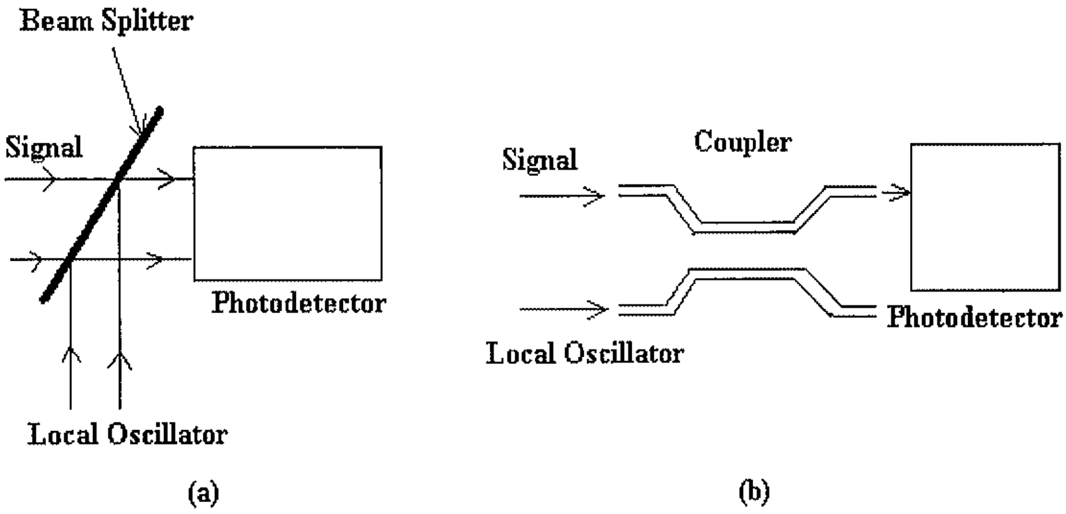

Figure 2.1 Optical heterodyne detection. A signal wave of frequency ν_s is mixed with a local oscillator wave of frequency ν_L using (a) a beam splitter, and (b) an optical coupler. The photocurrent varies at the frequency difference $\nu_I = \nu_s - \nu_L$.

(Taken from Figure 22.5-1, Reference [13])

The mathematics of the electric field mixing can be understood as follows: Express the signal optical field as $E_s = \mathrm{Re}\{A_s \exp(j2\pi\nu_s t)\}$ where $A_s = |A_s|\exp(j\varphi_s)$. In this expression, $|A_s|$ stands for the magnitude, φ_s the phase, while ν_s is the frequency of the signal. Similarly, the local oscillator signal is expressed as $E_L = \mathrm{Re}\{A_L \exp(j2\pi\nu_L t)\}$ where $A_L = |A_L|\exp(j\varphi_L)$. These two signals are mixed together onto the photodetector by the use of a beam splitter or an optical coupler. Thus, on the photodetector, the total field is the sum of these two fields. So the absolute square value of the mixed signal can be expressed as:

$$\begin{aligned} |E|^2 &= |E_s + E_L|^2 = |A_s \exp(j2\pi\nu_s t) + A_L \exp(j2\pi\nu_L t)|^2 \\ &= |A_s|^2 + |A_L|^2 + 2|A_s||A_L|\cos[2\pi(\nu_s - \nu_L)t + (\varphi_s - \varphi_L)] \end{aligned} \qquad [2.1]$$

Since the intensity of light is proportional to the absolute-square values of the magnitude, the intensity of the mixed signals within the photodetector can be expressed as

$$I = I_s + I_L + 2(I_s I_L)^{1/2}\cos[2\pi\nu_l t + (\varphi_s - \varphi_L)]. \qquad [2.2]$$

In the above, ν_l is the frequency difference between the input and reference signals.

The magnitude of photocurrent generated within the photodetector is proportional to the incident optical intensity. If the frequency difference ν_l is much smaller than the frequencies of both the input and the reference signals, then the mixed light is nearly quasi-monochromatic. The incident photon flux Φ is proportional to the incident optical intensity I, and is given as $\Phi \approx I/\eta\bar{\nu}$, where $\bar{\nu}$ is equal to $\frac{1}{2}(\nu_s + \nu_L)$. Therefore, the mean photocurrent i is given as: $i = \eta e\Phi = \eta e I/\eta\bar{\nu}$, where e is the electron charge and η

the photodetector's quantum efficiency to convert an incident photon into a photocarrier. Hence, the following expression shows the results for the photocurrent as

$$\bar{i} = \bar{i}_s + \bar{i}_L + 2(\bar{i}_s \bar{i}_L)^{1/2} \cos[2\pi \nu_I t + (\varphi_s - \varphi_L)]. \qquad [2.3]$$

Where $\bar{i}_s = \eta e I_s / \eta \bar{\nu}$ is the mean photocurrent generated by the input signal and $\bar{i}_L = \eta e I_L / \eta \bar{\nu}$ is the mean photocurrent generated by the local-oscillator signal. Figure 2.2 shows an example of the photocurrent generated by the photodetector. We can see that the current is oscillating at the difference frequency. The input signal's magnitude ($\bar{i}_s$) and phase (φ_s) are also available from the diagram, since these quantities modulate the detected current in magnitude and phase individually. By using the conventional techniques used in AM/FM radio receivers, the complete input signal information can be obtained. The demodulation can, in principle, be performed by any non-linear element such as a square-law device, a Schottky diode or a varistor [14].

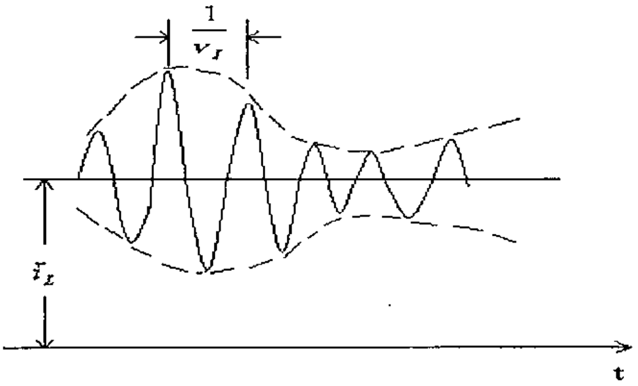

Figure 2.2 Photocurrent generated by the heterodyne detector.

(Taken from Figure 22.5-2, Reference[13])

2.3 Experimental Background and Review

Photoheterodyne technique has been used in the area of coherent detection for a few years based on the physics discussed in the previous section [15,16]. More recently, the photomixing technique has also been proposed as a means for coherent microwave and millimeter-wave generation. In principle, such a scheme can provide output signal at any desired difference frequency, making it a very versatile frequency generation technique. This idea becomes more important given the lack of tunable solid state coherent sources operating with fundamental frequencies above the GHz range. For example, while the resonant tunneling diodes and other quantum well structures have been proposed to operate at such high frequencies, their useful range is easily curtailed by the presence of parasitic resistances that offset the internal negative device resistance [17]. There are some other alternatives such as three-wave mixing in non-linear crystal, which can be used to generate coherent radiation. However, this process has a very stringent requirement on maintaining phase matching, and hence is not very convenient or realistic [18].

However, interests in the coherent generation by optical heterodyning remained low for many years due to the lack of robust high-quality tunable optical sources and reproducible device structures. Besides the poor reliability, the output power is limited to the microwatt range, which greatly reduces its application. However, with the advent of new stable, tunable lasers and the development of GaAs based technology, this picture has begun to change.

The following schemes have been proposed for obtaining coherent radiation from semiconductors:

(I) The incidence of a photon flux on the surface of a direct bandgap material having high carrier mobility such as GaAs [5-7,19]. Electron-hole pairs are then generated in response to the incident photon flux. Most of them are at or close to the surface. Band bending at the surface due to the presence of surface states provides a large internal electric field. The photogenerated carriers are thus made to move with large acceleration provided by the built-in surface electric fields. Their movements are in opposite directions, but the rapid acceleration provides for coherent radiative output. The advantages of this scheme are its inherent simplicity and lack of external biasing circuitry. However, the radiative propagation is not very anisotropic, and hence the output from the top exposed surface is not very significant. Besides, carriers generated deeper into the GaAs material do not contribute much to the radiation as the electric fields and hence the acceleration is much weaker. Finally, continuous operation is not possible, as the photogenerated carriers tend to quench the surface electric field.

Other similar concepts have used quantum well structures to produce radiation following an initial photoexcitation process [20]. The photoexcitation creates carriers, which remain trapped in two adjacent quantum wells. With time, the trapped charge swaps back and forth between the two quantum wells, thus producing the internal oscillating currents necessary for radiation. Though much faster, this scheme again suffers from the drawback of efficient optical channeling to the outside.

(II) The incidence of two coherent electromagnetic signals on a direct bandgap, biased semiconductor (such as GaAs) produces internal photocurrents. The photocurrents then act as distributed sources for radiation in accordance with Maxwell equations. The radiation from the illuminated GaAs material, however, is nearly isotropic. Appropriate lenses and waveguides are often necessary to efficiently focus and collect the generated radiation [21]. As a result, the overall radiative efficiency of such a scheme is not very good.

(III) Finally, the most efficient technique, in terms of its radiative output is a variation of the two-signal photomixing approach. Instead of direct radiation from the GaAs photomixer element, the generated currents are fed to appropriate impedance matched antenna structures [22,23]. The electromagnetic radiation can then be obtained in a directed manner. Given the advantage of this approach, it has been proposed for the NASA application.

A direct bandgap semiconductor (usually GaAs) serves as the photomixing medium for maximum optical absorption. The high carrier mobilities of GaAs serve to enhance the internal photocurrent magnitudes. Interdigitated GaAs metal-semiconductor-metal (MSM) structures are becoming increasingly attractive as the photomixing elements due to their numerous advantages. These advantages include compatibility with planar field effect transistor technology, low voltage operation, negligible leakage currents and capacitances that are smaller than in other vertical structures.

2.3.1 Summary of Reported Data and Results

S.Y. Chou et al. [24] have successfully fabricated GaAs MSM photodetectors by using high-resolution electron beam lithography. These interdigitated device structures serve as the basic mixing elements, and their dimensions have been in the micron range. The reported dark currents were as low as 40nA with a 0.5 V bias applied to an

$14.5\mu m \times 15\mu m$ area. At the wavelength of 632.8nm, the devices provided a sensitivity of about 0.2A/W. It was also shown that the response time decreased dramatically for finger spacing lower than 0.3 μm. This was explained as being the result of ballistic transport. Thus, as the finger spacing became comparable to the mean free path, the carriers encountered much less scattering before traveling through the space between any two fingers. It was also shown that the detector capacitance depended on the ratio of the finger width to their spacing period. A smaller ratio resulted in faster response. Finally, a biasing dependence was observed. The conclusions were that increasing the applied voltage enhanced the frequency response provided the breakdown field threshold was not exceeded.

Since the early 1990's, a group at the MIT Lincoln Laboratory led by E.R. Brown and K.A. McIntosh has been working on the fabrication of LTG (low temperature grown) GaAs inter-digitated photomixers for generating coherent radiation. In 1992, the highest output power of 200 μW at a frequency of 200MHz was attained [25]. The conversion efficiency was 0.14 per cent, and the highest frequency response was about 25GHz, limited by the parasitic capacitances. In 1993, they fabricated a new photomixer with smaller 0.6 μm gaps, which could generate up to 0.1 mW microwave output at a 0.2 GHz frequency under room temperature operation [26]. At a lower temperature of 77K, the radiation power was much higher at about 4mW. In order to increase the cutoff frequency even further, LTG-GaAs material with a 0.27 ps recombination time was subsequently used to make a similar device [23]. A working frequency as high as 3.8 THz was reported. In this device, a three-turn self-complementary spiral antenna was added for radiating the electromagnetic power into free space. The reported data showed the output power to be approximately 0.035mW at 20GHz and to remain flat up to about 300GHz. It then decreased at an approximate rate of 12dB/oct. beyond 300 GHz.

In 1995, this device was improved further to work up at frequencies up to 5 THz with a 3dB bandwidth of 650GHz high [27]. The 3dB bandwidth was shown to be independent of the pump laser wavelength from 780nm to 850nm. But for pumping wavelengths shorter than 750nm, the bandwidth was reduced significantly. The authors suggested that the reason should be the intervalley transfer effect. At the shorter pumping laser wavelengths, the photogenerated carriers have higher energy, and the probability for the excited carriers undergoing an intervalley transfer process increases. As a result, more carriers reside in the longer lifetime states within the satellite valleys. They cannot be trapped as easily at the arsenic-related midgap states. The final effect is that the average lifetime of the carriers increases, causing the response to be less sensitive at high frequency, i.e. the bandwidth is effectively reduced.

2.3.2 Material Characteristics

As discussed in the previous section, the trend for performance enhancement has been to fabricate the basic photomixer element from LTG-GaAs material. The use of LTG-GaAs has shown to increase the frequency characteristics. The reason of choosing this low-temperature-grown GaAs material is associated with its remarkable optoelectronics properties.

First, the LTG material has a much higher density of internal defects, which dramatically lowers the carrier lifetime. As a result of the sub-picosecond recombination times, devices made from this material can respond to high frequency optical signals by facilitating rapid variations in the photocurrent. This enhances not only the frequency response, but also the radiation since electromagnetic output is created by an oscillating current. However, short recombination times lead to low density of photogenerated carriers, which implies low sensitivity. Fortunately, LTG-GaAs has a very high photocarrier mobility (about $200cm^2V^{-1}\sec^{-1}$) which compensates the negative effect of a short recombination time on the sensitivity. The disadvantages of short recombination time are the higher internal heating and enhanced incident optical power levels.

Second, LTG GaAs material has a very high breakdown field ($E_B > 4\times10^5 Vcm^{-1}$) which permits the application of large device voltages, causing greater acceleration of the photogenerated carriers and subsequently larger radiation.

Finally, this material has very high resistivity due to the high density of internal traps which minimizes dark currents. So the transitions between the ON and OFF states of this device are very sharp and well separated.

2.3.3 Smaller Device Dimensions

Most of the recent research work mentioned above has used GaAs material with feature lengths in the micron range. But according to the conclusion made by S.Y. Chou et al. [24], reducing the feature size to nanoscale dimension can potentially enhance the optical heterodyne performance. The improvements in the performance are expected to be in the temporal response and in terms of higher cut-off frequencies. The smaller device dimensions would facilitate shorter transit times with possible ballistic carrier transport, lower the capacitances, and increase the internal electric fields for driving the carriers faster.

2.3.4 Device Geometry and Antenna Structures

The optical heterodyne devices reported to date usually use interdigitated GaAs metal-semiconductor-metal (MSM) structures because they can operate at lower voltages with negligible leakage currents, and have capacitances much smaller than those of other vertical structures. The electrodes are often connected to an antenna structure in order to enhance the radiation efficiency. Figure 2.3 is a typical optical heterodyne device structure taken from a reported publication by Brown et al. [23].

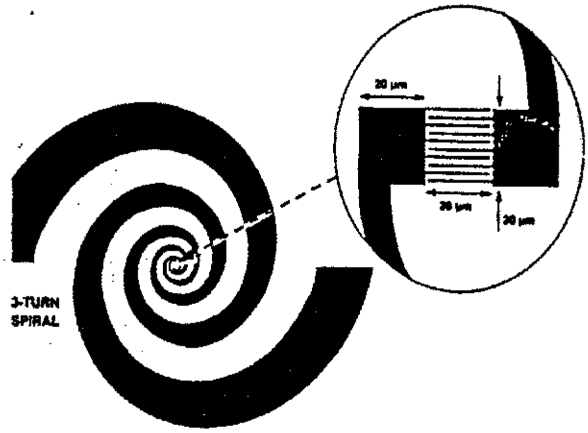

Figure 2.3 Three-turn, self-complementary spiral antenna photomixer structure.

(Taken from Figure 1, Reference[23])

2.4 Simulation Methods

Although many experiments have been done on the optical heterodyne devices, there is still a lack of theoretical study. However, numerical simulations could lead to a better understanding of the underlying physics, be useful in accurate predictions of the device performance and potential limitations, and be a convenient tool for design optimization. Such modeling can also yield detailed predictions on the power output capability, the conversion efficiency as a function of frequency, wavelength and operating temperature, and the internal heat generation levels. Usually, such information is not easy to obtain, either because the complicated instrumentation is involved or because the observed macroscopic effects are an integrated result of several ongoing processes. It is therefore, often difficult to separate the contributions and the roles of the different processes.

The only modeling work carried out to date that directly relates to the LTG GaAs based photomixers has been done by Brown et al. [28]. A numerical scheme based on the drift-diffusion approach was used. However, as is well known, this method is inadequate for modeling electronic transport in ultra-small semiconductor structures. It also fails in the high frequency regime, and does not take account of the electromagnetic aspects.

The Monte-Carlo (MC) method [36, 37] can provide a more accurate and direct analysis of ultra-fast transient phenomena inside the semiconductor. It can also incorporate effects that arise from high electric fields and small dimensions. To date, no Monte Carlo calculation has been carried out for the two-laser input optical heterodyne mixer system. However, the MC method has been applied to calculations of the photoresponse of single optical inputs onto GaAs [29-31]. Both normal GaAs and the LTG material were investigated. However, these simulations have all treated only the carrier transport issue. Also, only the impulse response was simulated rather than the behavior of more realistic sinusoidal optical waveforms. Furthermore, the electromagnetic aspect has been completely neglected in all previous calculations. This assumption of a quasi-static field is inadequate since both the optical signals and photocurrent inside the semiconductor do oscillate at a very high frequency. Given the THz frequency range of interest, one neither can ignore the large changes of the internal electrical field, nor can avoid the wave propagation aspects and the electromagnetic energy exchanges. It therefore becomes necessary to incorporate methods to update the electro-magnetic fields in parallel with the Monte-Carlo transport simulations. This is the main goal of this thesis, and the details are given in the next chapter.

CHAPTER III

SIMULATION TECHNIQUE AND NUMERICAL DETAILS

3.1 Introduction

As discussed in Chapter 1, optical heterodyning is proposed for the generation of coherent radiation in the terahertz region [32]. The main idea of the optical heterodyne process is simple. GaAs, a direct bandgap semiconductor is used as the photomixing medium, on which two laser beams with identical polarization and small frequency difference combine spatially. The optically generated electron-hole pairs inside the semiconductor produce a photocurrent, which is modulated at the difference frequency. This high frequency photocurrent can act as a distributed source of electromagnetic radiation, and can also be used to drive special antenna structures for more efficient radiation. This chapter presents details of the overall simulation technique used for modeling the photocurrent and radiative output from a GaAs photomixer. After describing the numerical approach, results obtained on the basis of this simulation scheme will be presented and discussed in the next chapter.

In order to simulate the photomixer response accurately in the terahertz range, details of carrier transport inside the semiconductor and the electromagnetic field propagation must both be carefully taken into account [33]. Here, the ensemble Monte-Carlo (MC) technique is used to physically model the carrier transport inside the semiconductor, while details of the electromagnetic field propagation are simulated directly by the full Maxwell equations. These two simulations interact with each other in the following coupled "leap-frog" manner: the full set of Maxwell equations gives the electromagnetic-field values under which the MC method simulates the carrier transport process. This electromagnetic field information is used by the MC method to provide current densities based on microscopic carrier movement. This current density information is then fed back into the full Maxwell equations for updating the electromagnetic fields. This completes one interactive, coupled leapfrog cycle. For the overall simulation, this coupled cyclical process is repeated over and over until the end of the total simulation time. It should be noted that the electromagnetic fields simulated by the Maxwell equations are affected by the global current generated by an ensemble of particles, but not by the current generated due to individual particles.

In the following sections, a few of the important numerical techniques for simulation of semiconductors are briefly described. Then, the Monte Carlo method used here for simulating transport of the photogenerated electron-hole pairs is discussed. This is followed by appropriate simple examples to demonstrate the accurate and correct numerical implementation of the MC technique. The subsequent section after the Monte Carlo discussion outlines the electromagnetic approach, and the coupling between the Maxwell equations and the MC scheme. Again simple examples have been given and discussed to show the correct implementation of the Maxwell equations in the time domain.

3.2 Numerical Simulation Techniques

The principal goal of semiconductor device simulations is to determine the behavior of terminal current and device voltage in response to an external bias, an optical excitation, or a thermal perturbation as a function of time. The mathematical model to be used for device analysis should in general include the dynamics of free carriers within the bulk semiconductor. It also should apply appropriate boundary conditions to different semiconductor sections, and account for the time dependent behavior at the contacts and surfaces and any applicable thermal exchange within the semiconductor system. The simplest approach for describing the transport behavior in semiconductors would be a classical Kinetic Approach. The kinetics of an "average particle" with a simple treatment of collisions to describe its motion could be used [34]. Though this approach would reasonably describe some macroscopic properties, all of the off-equilibrium effects are largely excluded.

A more sophisticated method of analysis has been based on using the Boltzmann Transport equation (BTE). The BTE, under several assumptions, can be simplified down into a relatively straightforward expression, known as the Drift-Diffusion equation. The drift-diffusion approach therefore is more approximate than the BTE, and suffers from all of its disadvantages. In the BTE scheme, a governing integro-differential equation is obtained from the distribution function f(r,p,t) of particle ensemble [35]. This distribution function f is the probability of finding a particle with the momentum p at a position r at time t. The BTE incorporates all of the internal scattering effects taking place over time. It is also able to describe transient effects correctly provided the scattering relationship can be characterized. Time-dependent perturbation theory based on the Fermi Golden rule is used to evaluate the scattering relationships. However, the Boltzmann transport approach is usually restricted to inherent assumptions of the distribution functions. This approach fails, however, in cases where simplified distribution does not exist, such as in a very short dimensional structure or during some ultra-short transient time intervals. Under high fields or nonlinear response conditions, the BTE has to be linearized. Because of this adjustment, it is not clear whether the features of the results are due to the microscopic model or they are due to the mathematical approximations.

However, before 1966, the theoretical model for simulating carrier transport processes in semiconductors and gas discharges was mainly based on the BTE. In order to simulate semiconductor structures correctly with very small dimensions, for phenomena involving ultra-short time scales, or when the assumptions of the BTE become unacceptable, another approach called the Monte Carlo Approach is used for greater accuracy [36]. This numerical approach was presented at the Kyoto Semiconductor conference in 1966, and is equivalent to the solution of the Boltzmann equation. In this stochastic Monte Carlo approach, individual particles are randomly selected and their motion followed in space and time. The average ensemble behavior is subsequently determined by collecting enough information about the particles. The biggest advantage of this method is that no fitting parameter is required. However, the approach is very intensively computational since a large number of particles are required to yield reliable statistics. The Monte Carlo technique is very popular and easy to implement. It offers the following advantages:

*The microscopic interpretation of the physical details is very transparent.

*Stochastic calculation is achieved at a minimum level of difficulty while incorporating memory effects.

*Temperature gradients and fields (both electric and magnetic) can all be comprehensively included.

*Time and space dependent phenomena can be easily simulated.

*No arbitrary assumption regarding the distribution function needs to be made.

*Arbitrary shapes and geometries, as well as complicated boundary conditions can be analyzed with ease.

Since the Monte Carlo method is a "direct" simulation method, both its final result and intermediate solution provide spatial and temporal microscopic information about the system. Thus, Monte Carlo can be used as an experimental technique, which provides more details than what the real experiments can provide. For example, it can be used to simulate physical situations unattainable in real experiments, or even investigate nonexistent materials in order to emphasize special features of the phenomenon under study.

3.3 Monte Carlo Simulation Method

3.3.1 The Ensemble Particle Monte Carlo Method

The details of the ensemble Monte Carlo (EMC) method are given in this section. These details have been taken from a review paper by Jacoboni and Reggiani [37]. The simulation starts with the particle in a given initial condition. The particle then flies freely unless it is perturbed by a scattering event caused by impurities, phonons, imperfections or other carriers. Therefore the duration of the free flight is chosen according to the scattering probabilities. During the free flight, the particle obeys classical laws of motion and its wave vector changes at the rate determined by the electric field E as:

$$k(t) = k_0 + \frac{qE}{\eta}t \ . \qquad [3.1]$$

where k is the wave vector at the end of the free flight, q is the charge with sign ($q<0$ for electrons and $q>0$ for holes). And η is the Plank constant divided by 2π. At the end of the free flight, a scattering mechanism is chosen according to the relative probabilities of all possible scattering mechanisms. Following the chosen scattering mechanism, the energy of the particle may change if it is an inelastic process. Meanwhile, the momentum components of the particle will be determined by the properties of the scattering mechanism. This new state after scattering will be the initial state for the next new free flight and this process is repeated. Figure 3.1 shows a basic structure of the Monte Carlo program, which will be discussed in detail by the following text.

At the first stage, a particle is given an initial momentum k and position at t=0, and then drifts freely in the semiconductor. So this stage calculates the duration time of the free flight.

Since the free flight is only disturbed by scattering events, the duration time depends on the scattering probability. For each scattering process, the transition rate from the momentum state $\eta k'$ to ηk is described as $S_n(k,k')$. Where the subscript n represents an individual scattering process which can take values from 1 to N (N is the total number of possible processes). So the total scattering rate from state k is given as:

$$\lambda(k)=\sum_{n=1}^{N}\lambda_n(k)=\sum_{n=1}^{N}\int S_n(k,k')dk' \ . \qquad [3.2]$$

According to equation [3.2], $\lambda(k)$ is the probability that a particle in the state k suffers a collision during the interval dt. Since the wave vector k of the particle changes continuously during its free flight under the applied field, the probability that an electron which suffered a collision at time t=0 has not yet suffered another collision after a time "t" is calculated through an integration over time as:

$$\exp(-\int_0^t \lambda[k(t')]dt') \ . \qquad [3.3]$$

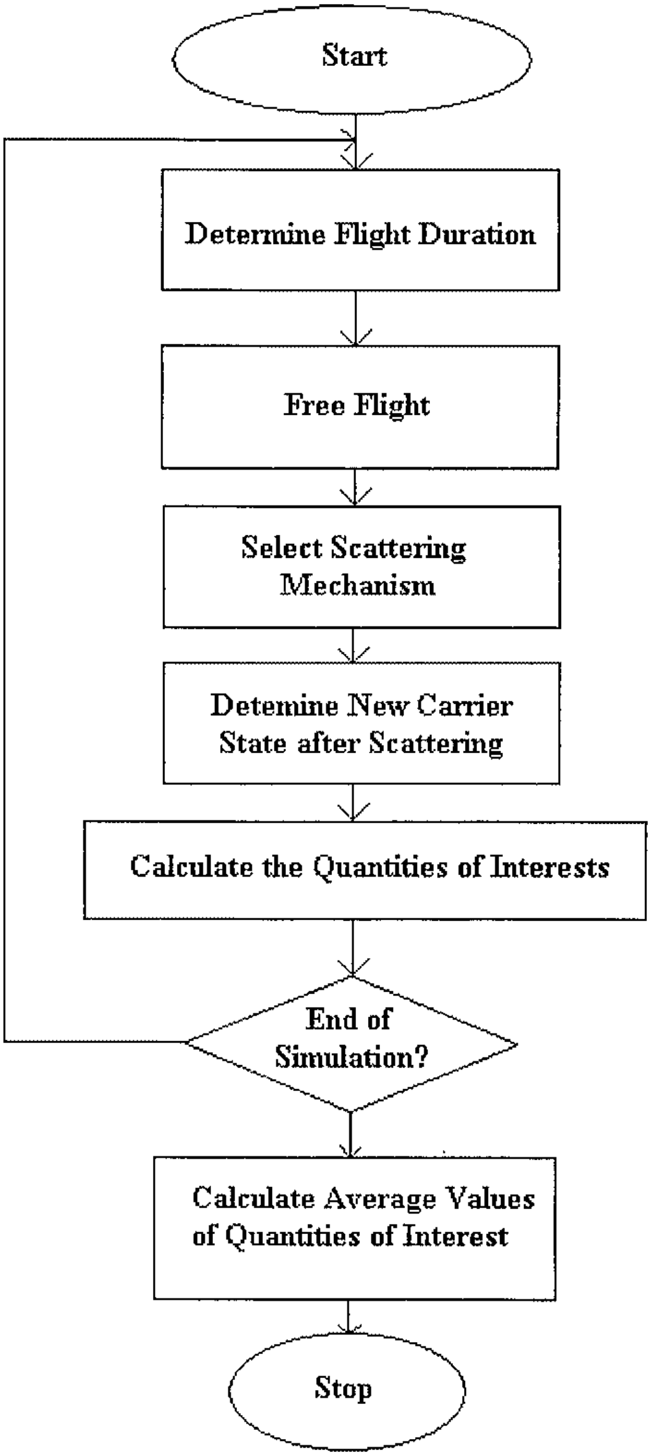

Figure 3.1 Flow chart of a simple ensemble Monte Carlo simulation program.

Therefore, the probability P(t) that the electron will suffer its next collision during the time interval dt around t is given by

$$P(t)dt = \lambda[k(t)] \cdot \exp(-\int_0^t \lambda[k(t')]dt') \cdot dt \ . \qquad [3.4]$$

According to its definition, the particle will definitely undergo a scattering event sooner or later, so we know that

$$\int_0^\infty P(t)dt = 1 \ . \qquad [3.5]$$

In the program, this complex distribution is simplified by mapping it onto a simple pseudo-random distribution. The most convenient pseudo-random distribution is the uniform distribution, which is readily available on most computer systems. This mapping relation is given as:

$$\frac{\int_a^q p(q')dq'}{\int_a^b p(q')dq'} = \int_0^r p(r')dr' \ . \qquad [3.6]$$

Where p(q) and p(r) are the respective probability densities, associated with q in the physical distribution and r in the pseudo-random distribution. In equation [3.6], a and b stand for the maximum and minimum value of q. Since p(r)=1 in the uniform distribution, we can get

$$r = \frac{\int_a^q p(q')dq'}{\int_a^b p(q')dq'} \ . \qquad [3.7]$$

So, according to equation [3.4], [3.5] and [3.7], a uniformly distributed random number r between 0 and 1 can be used to obtain the time point t at which the scattering event happens as:

$$r = 1 - \exp(-\int_0^t \lambda[k(t')]dt') . \qquad [3.8]$$

As we can see, equation [3.8] is very complicated, so the free flight time t cannot be analytically calculated for practical scattering mechanism. It is possible to use numerical integration to produce r and t in a tabular form for each value of |k|, but this approach is time consuming and almost impractical.

To overcome this difficulty, Ree has devised a very simple method, which introduces a fictitious scattering mechanism [38]. It is clear that if the total scattering rate $\lambda[k(t)]$ equals to a constant Γ, equation [3.8] can be simplified to the elementary form as:

$$r = 1 - e^{-\Gamma t} . \qquad [3.9]$$

The introduced new fictitious "self-scattering" makes the total scattering probability to be a constant as:

$$\lambda_T(k) = \lambda(k) + \lambda_V(k) = \Gamma . \qquad [3.10]$$

Actually, this "self-scattering" process does not affect the state of the electron. If the carrier undergoes this process, its state k' after collision is the same as its state k before the collision. This means that the electron continues free flight without perturbation as if no scattering event happened.

With the constant total collision probability, the free flight time t can be derived from equation [3.8] as:

$$t = -\frac{1}{\Gamma}\ln(1-r)\ . \qquad [3.11a]$$

Since r is evenly distributed between 0 and 1, "r" has the same meaning as "1-r" in practical use. Thus, equation [3.11a] can also be written as

$$t = -\frac{1}{\Gamma}\ln r\ . \qquad [3.11b]$$

So the flight time t can be determined by the uniformly distributed random number r. It should be noted that Γ must be chosen to be the maximum value of $\lambda(k)$, because otherwise negative value for $\lambda_V(k)$ will be introduced.

This new method introduces more computational work on "self-scattering" events, but the simplification of the calculation of the free flight time reduces the total computing time.

In the second stage, the particle flies freely under the electric field. The wave vector k of the particle changes according to the Newton's law of motion as is expressed in equation [3.1]. The flight is terminated after the free flight time t, which is calculated in the first stage. The values of position, momentum and energy of the electron are recorded at the end of this step.

The third stage selects which scattering mechanism terminates the free flight. In this program, the scattering rates of the various mechanisms are tabulated as a function of energy and normalized by the constant total scattering rate Γ at the beginning of this program. That is, for a given energy E, the normalized probability for jth scattering mechanism is expressed as $P_j(E)/\Gamma$. The selection of scattering mechanism is simple and straightforward: after generating a random number between 0 and 1, if

$\sum_{i=1}^{i=j-1} P_i(E) < r < \sum_{i=1}^{i=j} P_i(E)$, then the jth scattering mechanism is chosen. If $r > \sum_{i=1}^{i=N} P_i(E)$, where N is the total number of scattering mechanism, then the self-scattering process occurs. This selection method is shown in Figure 3.2.

Once the scattering mechanism is chosen at the end of free flight, the new state k' after scattering must be determined. This is the work done by the fourth stage. For example, if a fictitious "self-scattering" mechanism is selected, k' must be equal to the former state k just before scattering. That means the flight is not terminated, and a new flight time Δt is calculated again in the first stage and added to t. On the contrary, if a real scattering event occurs, k' is chosen stochastically according to the differential cross section of that particular mechanism. The detailed scattering process will be discussed later in this paper.

In the ensemble MC method, a large number of particles are simulated in parallel for a sequence of short time intervals (depending on simulation situation, typically 1fs). Figure 3.3 shows the simulation situation of an ensemble consists of N particles. In this figure, each trajectory line represents a particle's movement in time and the circles on the line represent scattering events happened between two free flight period. At each observation time step, a set of variables such as position, velocity, and energy for each particle is calculated using the MC method. The average value of a quantity A at a certain time t for this ensemble of particles is defined as the ensemble average over the N particles of the system as:

$$< A >= \frac{1}{N} \sum_i A_i(t_i = t) \,. \qquad [3.12]$$

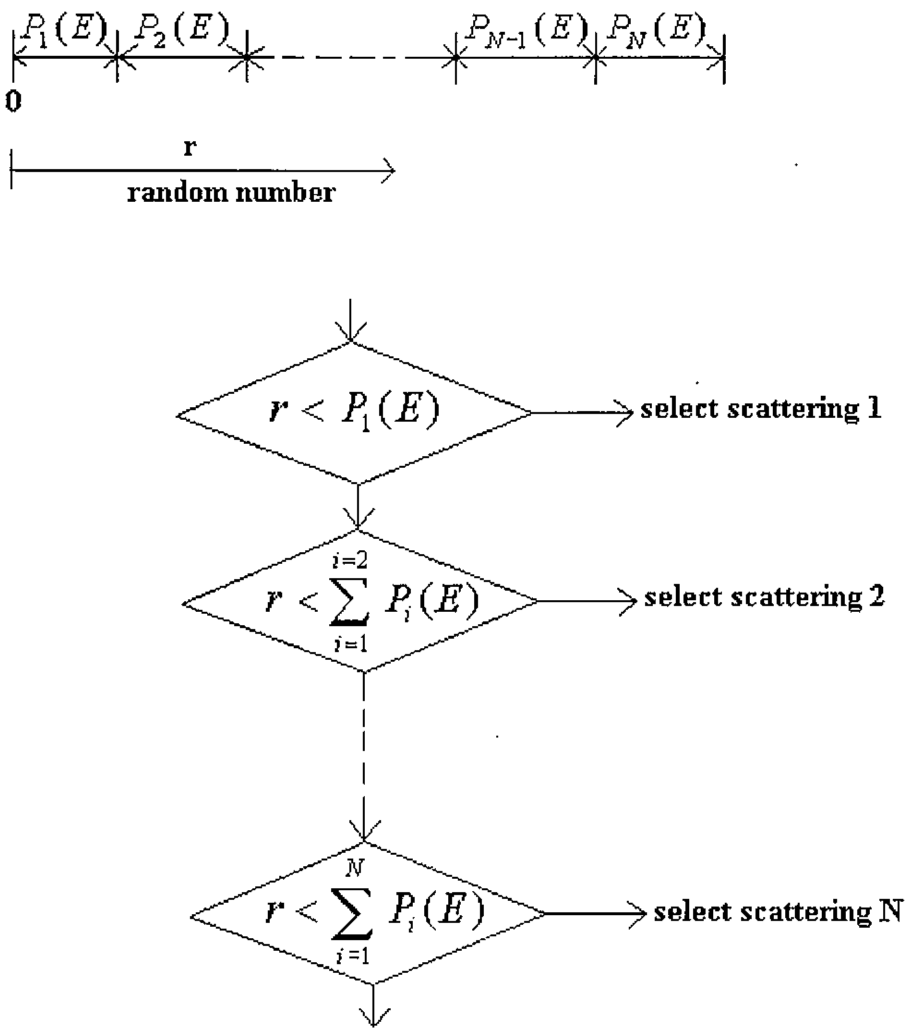

Figure 3.2 Flow chart of scattering mechanism selection in Monte Carlo simulation.

When the EMC method is used in practice, since the scattering events for each particle occur at different times from one another, a synchronization problem arises and is taken care in the fifth stage. In Figure 3.3 we can see that the observation times are represented by the label t(n) and t(n+1). Among the successive observation times, the whole system's status is computed by the MC method according to the following sequence:

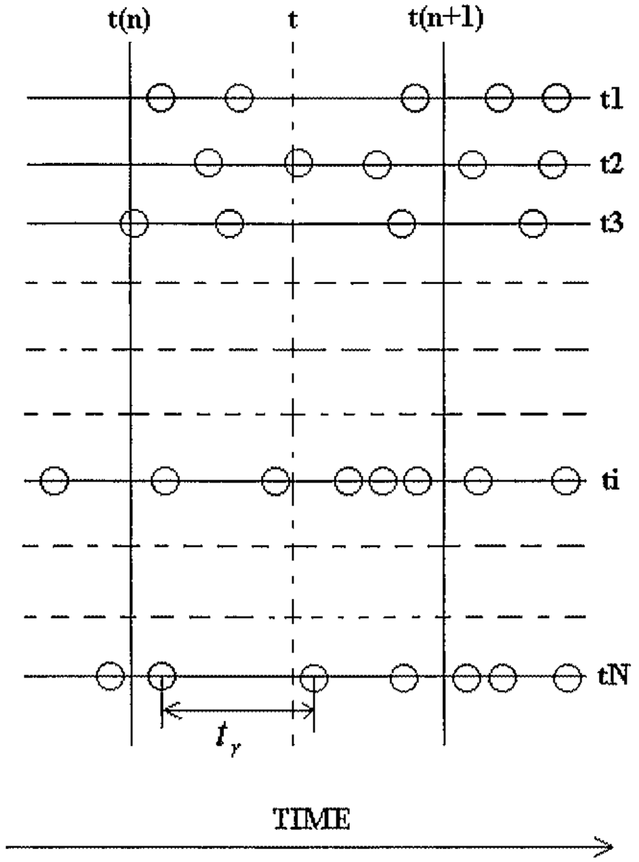

Figure 3.3 Example of ensemble Monte Carlo simulation where the time history of N carriers is recorded in parallel. t(n) and t(n+1) are observation points in time. The circles represent scattering events. (Taken from Figure 5, Reference [3.6])

a. The free flight time t_r is calculated according to Equation [3.11]

b. Increase the time variable t of each particle by t_r.

c. Compare the time variable t of each particle to t(n+1).

d. If $t < t(n+1)$, calculate the particle's new state at t. Then go to step a.

e. If $t > t(n+1)$, interrupt the free flight at t(n+1), calculate the new state of the particle at t(n+1). Do not allow scattering events take place.

f. The remainder of the free flight time t - t(n+1) is set to be the new free flight time and set the time variable of this particle to be t(n+1). Then go to step b for the next particle..

3.3.2 Scattering Mechanisms

In order to use the EMC to study the properties of semiconductor devices, the knowledge of the active scattering mechanism is required. The scattering events are caused by phonons, impurities, defects and other particles (electrons and holes). The particle will undergo a transition in status. If this transition is from one valley to another valley, it is called intervalley transition, otherwise it is called intravalley [39]. In this project, we consider only several scattering mechanisms: Polar-Optical Scattering, Non-equivalent Intervalley Scattering, Equivalent Intervalley Scattering, Intravalley Non-Polar-Optical Scattering, Piezoelectric Scattering, Acoustic Scattering and Ionized Impurity Scattering. The rates and properties of each scattering mechanism are given in Appendix A.

3.3.3 Test Results for MC Method

Figure 3.4 and Figure 3.5 show the energy dependence for the electron ionized impurity scattering rates at two different dopant densities, $1.0 \times 10^{15} / cc$ and

$1.0\times10^{16}\,/cc$. From these plots, we can see that the rates are higher at higher dopant density as we have expected. Another interesting thing is that the scattering rates increase with the energy, then they saturate and decrease when the energy is larger than a certain value. The saturation energy is larger when the dopant density is higher.

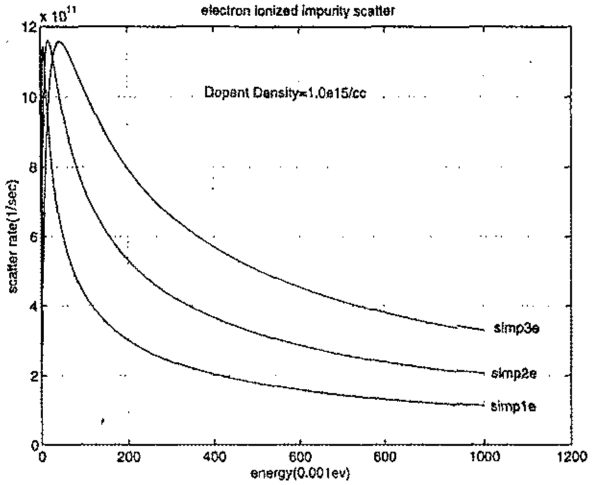

Figure 3.4 Ionized impurity scattering rate for electron at 1.0e15/cc dopant density.

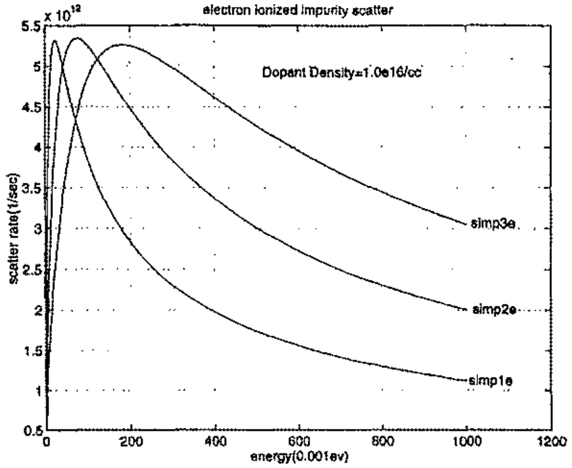

Figure 3.5 Ionized impurity scattering rate for electron at 1.0e16/cc dopant density.

Figure 3.6 shows the energy dependence for the electron equivalent intervalley scattering rate. From this plot, we can see all the emission scattering mechanisms have energy threshold because it is required for those electrons to have enough energy to generate phonons to the semiconductor lattice.

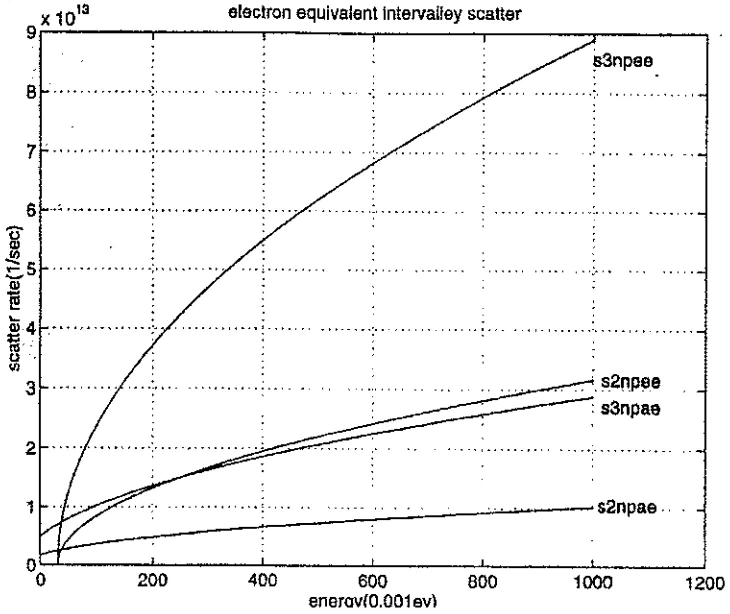

Figure 3.6 Equivalent intervalley scattering rate for electron.

Figure 3.7, 3.8 and 3.9 show the energy dependence for the electron non-equivalent intervalley scattering rate. From these plots we can see that some emission scattering mechanisms have threshold energy larger than the corresponding equivalent intervalley emission scattering mechanisms, because under such scattering mechanisms it is required for electrons to have an additional energy to jump from lower energy valley to higher energy valley ($\Gamma \rightarrow L, \Gamma \rightarrow X, L \rightarrow X$). Other emission scattering mechanisms do not have energy threshold because the electrons will gain enough energy to generate phonons when they jump from high energy valley to low energy valley ($X \rightarrow L, X \rightarrow \Gamma, L \rightarrow \Gamma$).

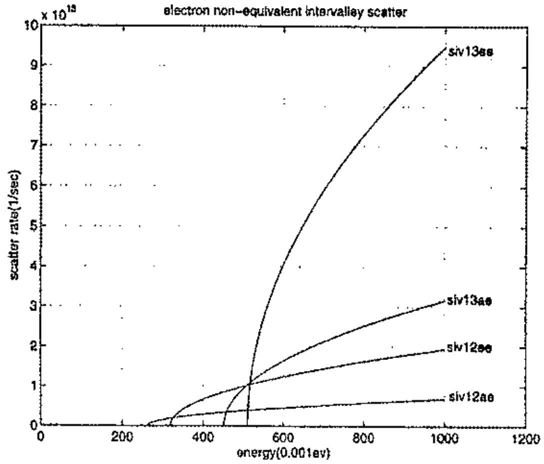

Figure 3.7 Non-equivalent intervalley scattering rate for electron.

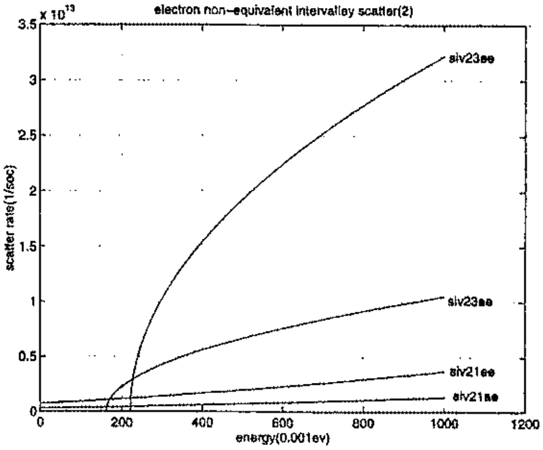

Figure 3.8 Non-equivalent intervalley scattering rate for electron(continued 1).

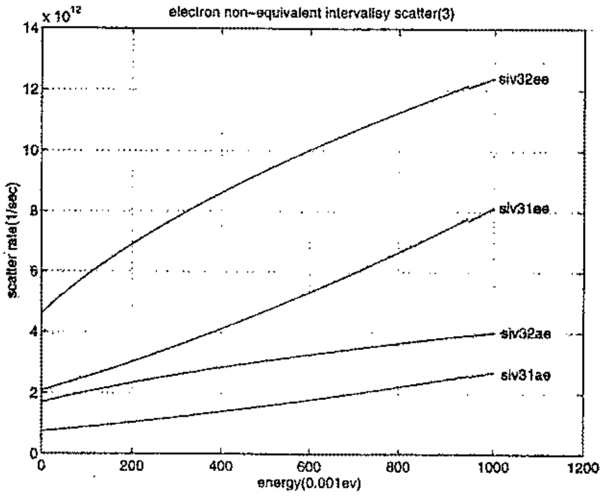

Figure 3.9 Non-equivalent intervalley scattering rate for electron(continued 2).

Figure 3.10 shows the energy dependence for the electron acoustic scattering rate. We can see that this scattering mechanism rate increases all the way when the electron energy goes up.

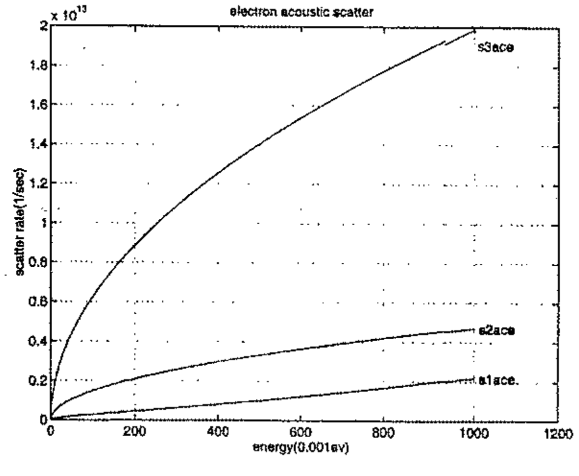

Figure 3.10 Acoustic scattering rate for electron.

Figure 3.11 shows the energy dependence for the electron polar optical scattering rate. We can see that the emission mechanism has energy threshold, and the scattering rate decreases when the electron energy is bigger than a certain value. Figure 3.12 shows the energy dependence of total scattering rate for electrons locating at different valley.

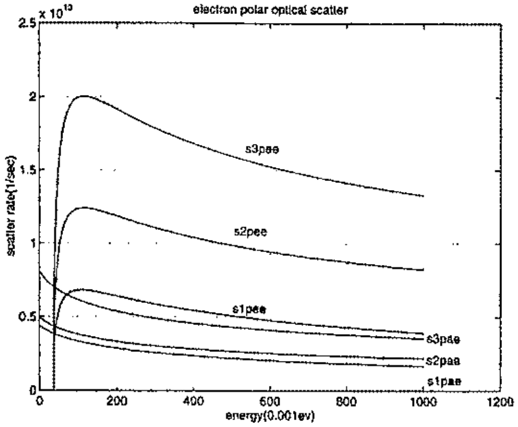

Figure 3.11 Polar optical scattering rate for electron.

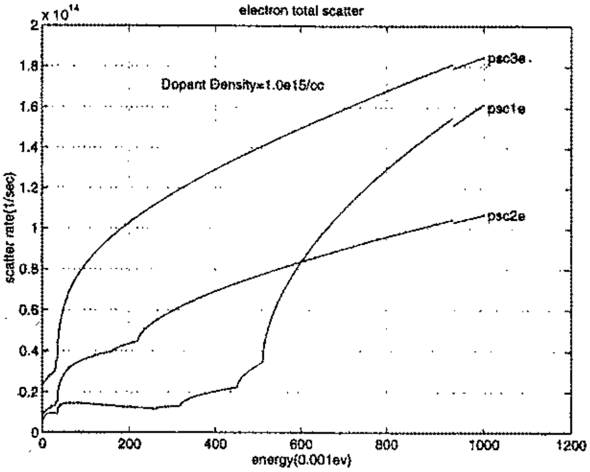

Figure 3.12 Total scattering rate for electron.

Figure 3.13~3.18 show the test result on several scattering mechanisms individually. In these tests, only one kind of scattering mechanism is chosen to take effect during the simulation. The condition for each of these simulation tests is the same: simulate 1000 electron hole pairs undergo 500 times of scattering events in the semiconductor. The initial velocity of each carriers is set to be $10^5 m/\sec$ at x direction and zero in both y and z direction. We also set 1/3 of the electrons in Γ valley, 1/3 in X valley and 1/3 in X valley.

Figure 13~14 show the simulation result when only the acoustic phonon scattering mechanism takes effect. It is clear from these plots that the result of the acoustic scattering mechanism is to randomize the velocity distribution of each carrier, so the average velocity of the carriers goes to zero in every direction no matter what the initial velocity distribution is. Meanwhile, we can also see that this mechanism is elastic, so the energy of the carriers remains the same throughout the simulation time.

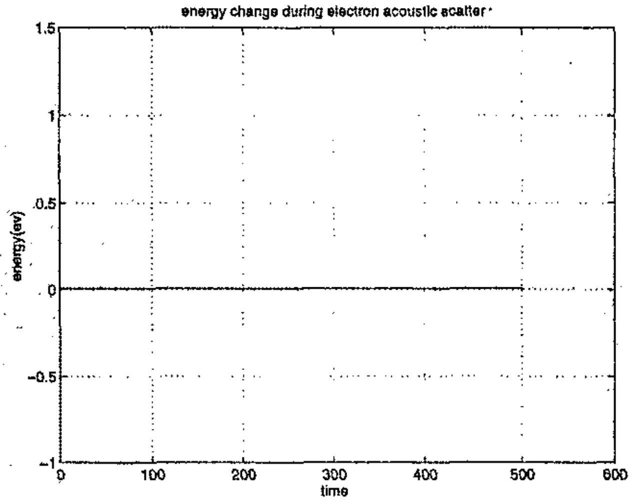

Figure 3.13 Electron energy development during acoustic scatter

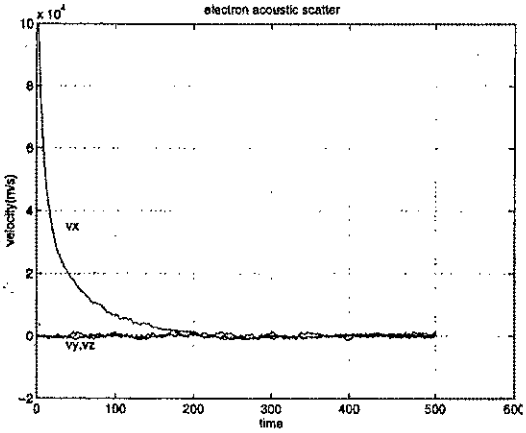

Figure 3.14 Electron velocity development during acoustic scatter.

Figure 15~16 show the simulation result for electron intervalley non-equivalent phonon scattering mechanisms. At this time, because of the participation of phonon absorption or emission, the energy of electron is changing during the simulation, which means this mechanism is inelastic. From these plots, we can see electron energy increases during this simulation because the phonon absorption dominates over emission due to the relatively low initial energy. This is also revealed in Figure 3.7. Also, we can see that this scattering mechanism does not randomize the distribution of final velocity completely. The velocity of electrons in the x direction does not go to zero. This occurs because 1/3 of the electrons are set to be in the Γ valley with an initial energy which is smaller than the energy difference between the Γ and X valleys or between the Γ and L valleys. Thus, under the zero field, these electrons can never gain enough energy to be able to make an intervalley transition even with the absorption of a phonon. Since no other scattering mechanisms take effect, these electrons never suffer any scattering event and keep on moving with the same initial velocity. Those in the L or X valley can scatter and hence randomize. From these analysis we would expect that the average velocity in x direction in the end should be 1/3 of the initial velocity. And this is proved from the results shown on these plots.

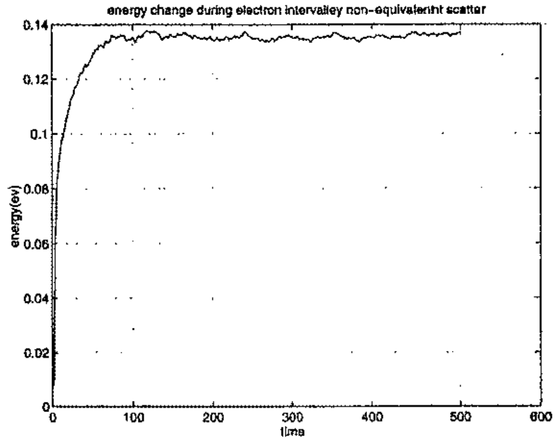

Figure 3.15 Electron energy development during intervalley non-equivalent scatter.

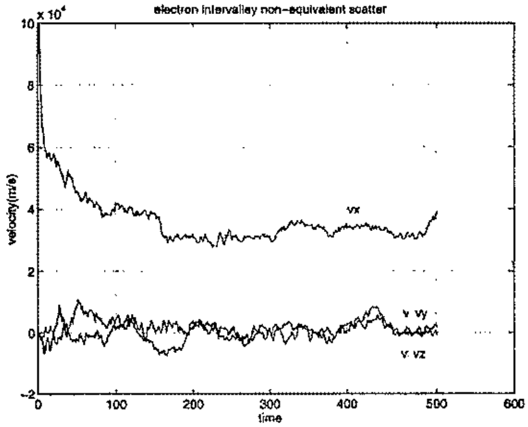

Figure 3.16 Electron velocity development during intervalley non-equivalent scatter.

Figure 3.17~3.18 are for the electron intervalley equivalent phonon scattering mechanism.

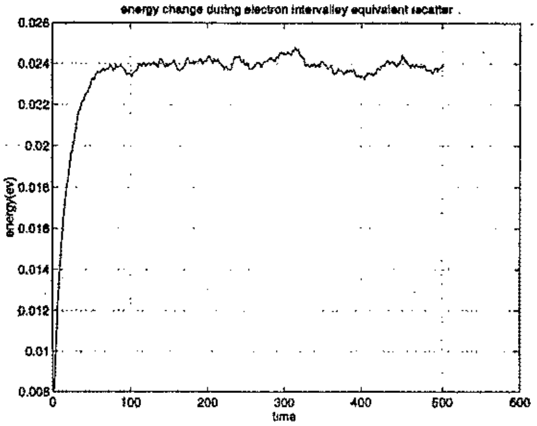

Figure 3.17 Electron energy development during intervalley equivalent scatter.

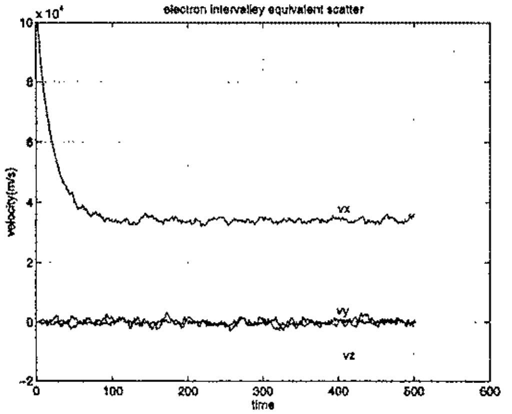

Figure 3.18 Electron velocity development during intervalley equivalent scatter

From the above plots, we can see that this mechanism is also an inelastic process. This mechanism does not randomize the velocity in x direction completely because the intervalley equivalent scattering mechanism can only happen between the L and X valleys. The velocity of electrons in these two valleys is randomized while the electrons in Γ valley do not suffer any scattering event during the simulation process. Thus, the velocity of electrons in x direction does not go to zero. From this analysis we would expect that the average velocity in x direction in the end should be 1/3 of the initial velocity. And this is proved from the results shown on these plots.

Figure 3.19 shows the simulation result on the time dependence of carrier drift velocity under different electric field.

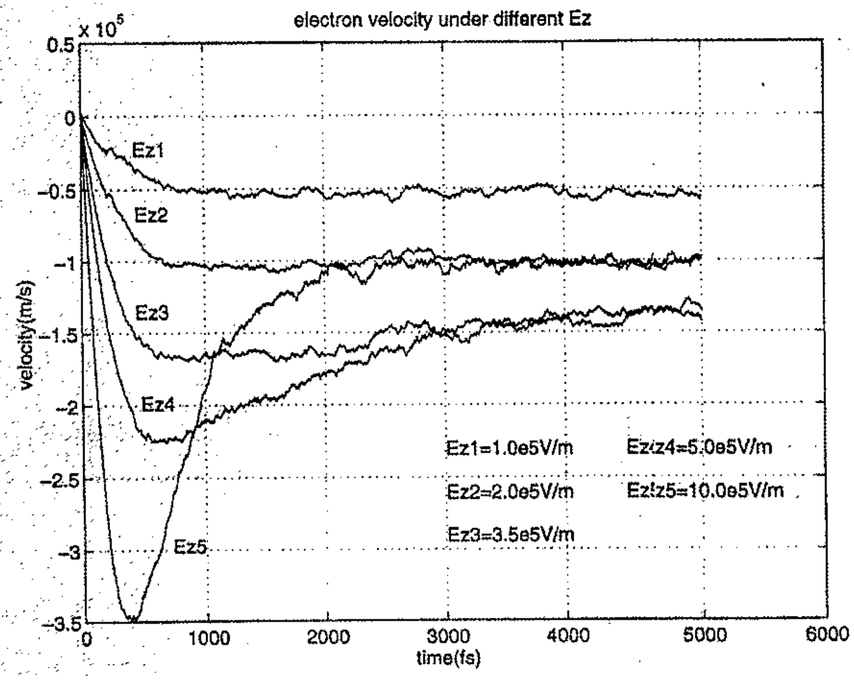

Figure 3.19 Time dependence of electron drift velocity

under different electric field.

We can see from this plot that the stabilized drift velocity of the electrons is increasing with the electric field when the field strength is small. But at larger electric field the electron velocity goes down when the field strength becomes higher than a certain value. This is the well-known Gunn effect [40] and can be easily understood. The higher the electric field, the higher is the probability of populating electrons in the X and L valleys which have higher effective mass than the Γ valley. As a result, a velocity overshoot results.

3.4 Full Maxwell Equations Simulation Method

3.4.1 Full Maxwell Equations Simulation

During the simulation process, the electro-magnetic field must be updated due to the movement of the charged carriers inside the semiconductor. Most semiconductor simulation methods used Poisson equation to update the electro-magnetic field inside the semiconductor and got satisfied results. In this thesis research, the radiated power from the semiconductor needs to be calculated which requires the information both on electric field and magnetic field. Unfortunately, the Poisson equation only updates the electric field according to the boundary condition and the charge density distribution. So it does not provide accurate magnetic field information which is needed to calculate the radiation. Thus, the full set of dynamic Maxwell equations needs to be used to update both the electric and magnetic field. The details of this simulation method are described below. And these details are taken from a paper by Xiaolei Zhang and Kenneth K. Mei [41].

In this project, we only consider two-dimensional problem and assume that the field is unchanged along z direction. See Figure 3.20, only three components of the electromagnetic field are considered, they are: Ex, Ey and Hz. Accordingly, the Maxwell equations for solving this two-dimensional problem become a set of three equations

$$\begin{aligned} \varepsilon_0 \frac{\partial Ex}{\partial t} + \sigma Ex &= \frac{\partial Hz}{\partial y} \\ \varepsilon_0 \frac{\partial Ey}{\partial t} + \sigma Ey &= \frac{\partial Hz}{\partial x} \\ \mu_0 \frac{\partial Hz}{\partial t} + \sigma^* Hz &= \frac{\partial Ey}{\partial x} - \frac{\partial Ex}{\partial y} \end{aligned} \quad . \qquad [3.13]$$

Where σ is the electric conductivity and σ^* is the magnetic conductivity. For the simulation in the semiconductor and vacuum region, we can calculate the current density distribution J_x and J_y according to the particles' distribution and velocity simulated by MC method and substitute them as the σE_x and σE_y respectively in equations [3.13]. The magnetic conductivity σ^* is zero for both vacuum and semiconductor.

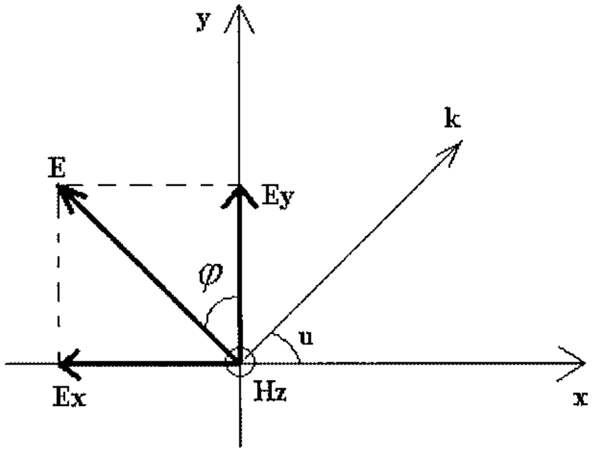

Figure 3.20 The transverse electric problem.

(Taken from Figure 1, Reference [46])

The numerical implementation of these three differential equations can be shown in Figure 3.21.

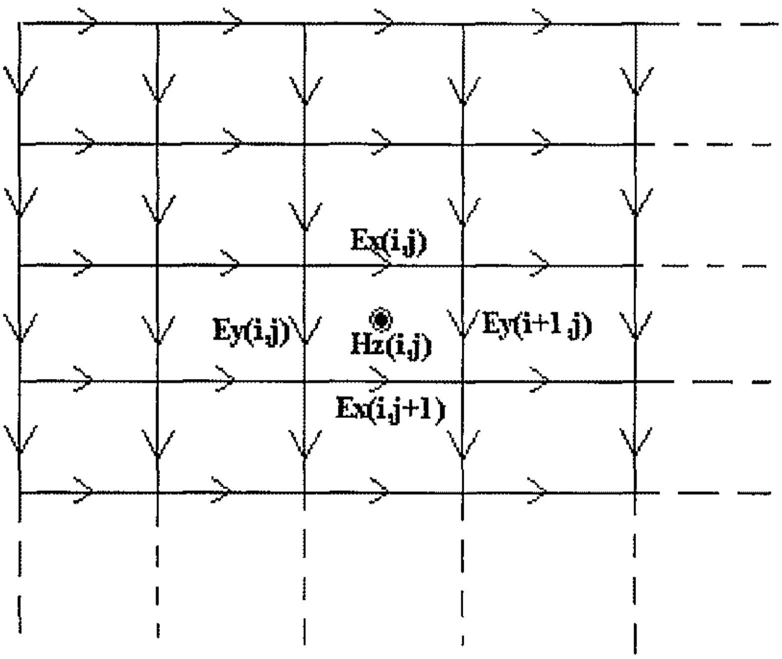

Figure 3.21 Full Maxwell equations method grid.

In this figure, the computational region is decomposed into a mesh of boxes which is labeled as (i,j). The electric field values are defined along the edge of each box. On the clockwise order from the top, the electric field is defined as Ex(i,j), Ey(i+1,j), Ex(i,j+1) and Ey(i,j). And the magnetic field is defined in the center of the box as Hz(i,j). In the numerical program code, the equations [3.13] are transformed into the following form which can be processed by computer as

$$\begin{aligned} Hz^{(n+1/2)}(i,j) &= Hz^{(n-1/2)}(i,j) + \\ &\quad \frac{\Delta t}{\mu_0}\left[\frac{Ex^{n}(i,j+1)-Ex^{n}(i,j)}{\Delta y} - \frac{Ey^{n}(i+1,j)-Ey^{n}(i,j)}{\Delta x}\right] \\ Ex^{(n+1)}(i,j) &= Ex^{(n)}(i,j) + \frac{\Delta t}{\varepsilon}\left[\frac{Hz^{(n+1/2)}(i,j)-Hz^{(n+1/2)}(i,j-1)}{\Delta y} - Jx(i,j)\right] \\ Ey^{(n+1)}(i,j) &= Ey^{(n)}(i,j) + \frac{\Delta t}{\varepsilon}\left[\frac{Hz^{(n+1/2)}(i,j)-Hz^{(n+1/2)}(i-1,j)}{\Delta x} - Jy(i,j)\right] \end{aligned} \qquad [3.14]$$

In this numerical process, the electric field and the magnetic field are not updated simultaneously, the chronology is shown in Figure 3.22.

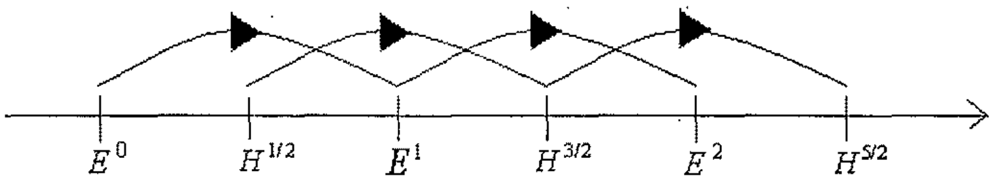

Figure 3.22 The full Maxwell equation simulation chronology.

The most difficult part of this simulation method is to choose and set the boundary conditions. As we can see, in the Poisson equation method, the boundary condition can be easily set as we know the potential value at the boundary. But in this full Maxwell equations method, the curl of E is not zero, so the scalar potential does not have any meaning in this case. Here a battery unit was introduced into the simulation system with a fixed internal electric field, and connected to the electrodes with two metal wires taken to have zero electric field inside. This configuration is shown in Figure 3.23. The tangential electric field was set equal to zero on all conducting sheets, contacts and metal wires.

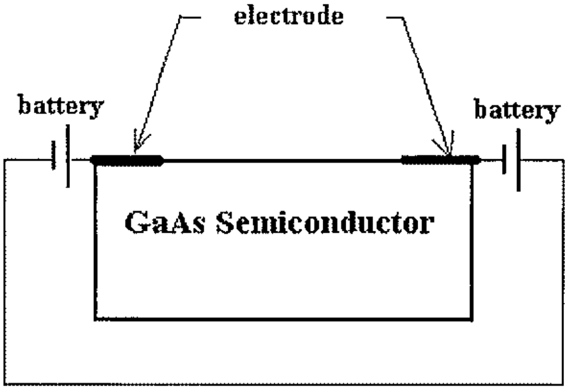

Figure 3.23 Boundary condition set in full Maxwell equation simulation.

3.4.2 Perfect Matched Absorbing Boundary

Work on the numerical implementation of Maxwell's equations was demonstrated by K. S. Yee in 1966 based on the finite difference time-domain technique [42]. However, there is a difficulty in implementing this technique for the general solution of Maxwell equations in free space: In computer simulation process, Maxwell equations must be solved within a restrained finite-size geometry, since no computer can provide memory for calculation over infinite space. Because the whole simulation cannot be done under an open (infinite) space status, the reflection of the electromagnetic wave from the system boundary chosen will cause undesired and unphysical energy accumulation inside the system. In order to eliminate this problem, some special techniques need to be used to make the boundary a "highly absorbing layer" to prevent back-reflection of energy. A number of numerical techniques have been devised for this purpose. One of these techniques is based on incorporating a "radiating boundary" [43]. However, this is difficult to implement since one needs to assign wavelength, and position dependent radiating boundary condition, which also depends on the angle of wave incidence. Another technique uses a matched absorbing layer whose impedance matches the free space [44]. Other mathematical "absorbing conditions" are derived from approaches first used for acoustic waves [45]. However, these schemes can absorb a wave without reflection only in particular cases, such as a plane wave perpendicularly hits the boundary.

The idea of the absorbing medium is quite simple. As we can see from the equation [3.13], if the condition

$$\frac{\sigma}{\varepsilon_0} = \frac{\sigma^*}{\mu_0} \qquad [3.15]$$

is satisfied, the impedance of this medium equals to that of vacuum. Thus, if a plane wave propagates normally across this vacuum-medium interface, no reflection will arise. Meanwhile, the nonzero conductivity in the medium forces the wave inside the medium to be absorbed. This is the basic idea of "matched absorbing medium". This simple idea is not perfect, however for all situations, because it cannot guarantee zero reflection for non-normal incidence.

In this thesis work, a new technique for constructing a better absorbing boundary layer derived recently by Jean-Pierre Berenger has been introduced [46]. With this new absorbing layer, if a plane wave hits this layer at any incident angle and frequency, no reflection arises. Thus, in theory, this absorbing boundary layer can absorb any wave traveling towards the boundary without reflection irrespective of its polarization, wavevector and incident angle. In all subsequent discussions here, we will call this layer as the perfectly matched layer (PML). The PML medium is treated slightly different from ordinary mediums in one respect: Its magnetic component Hz is deliberately broken into two subcomponents Hzx and Hzy. Hence, the electromagnetic field inside the PML medium has four components, Ex, Ey, Hzx and Hzy with the relationship shown by equations [3.16]. Where $\sigma_x, \sigma_x^*, \sigma_y$ and σ_y^* behave as the electric and magnetic conductivities in equations [3.13].

$$\begin{aligned}
&\varepsilon_0 \frac{\partial Ex}{\partial t} + \sigma_y Ex = \frac{\partial (Hzx + Hzy)}{\partial y} \\
&\varepsilon_0 \frac{\partial Ey}{\partial t} + \sigma_x Ey = -\frac{\partial (Hzx + Hzy)}{\partial x} \\
&\mu_0 \frac{\partial Hzx}{\partial t} + \sigma_x^* Hzx = -\frac{\partial Ey}{\partial x} \\
&\mu_0 \frac{\partial Hzy}{\partial t} + \sigma_y^* Hzy = \frac{\partial Ex}{\partial y}
\end{aligned} . \qquad [3.16]$$

Consider an electromagnetic wave propagating in the PML medium along a direction, which makes an angle with the y axis. The four components of the field can be written as

$$\begin{aligned}
&Ex = -E_0 \sin \varphi e^{i\omega(t - \alpha x - \beta y)} \\
&Ey = E_0 \cos \varphi e^{i\omega(t - \alpha x - \beta y)} \\
&Hzx = Hzx_0 e^{i\omega(t - \alpha x - \beta y)} \\
&Hzy = Hzy_0 e^{i\omega(t - \alpha x - \beta y)}
\end{aligned} . \qquad [3.17]$$

Where ω is the frequency of this wave. If both (σ_x, σ_x^*) and (σ_y, σ_y^*) satisfy the condition [3.15], substituting equations [3.17] into equations [3.16] yields the following expressions of the wave components and the impedance Z :

$$\begin{aligned}\psi &= \psi_0 e^{i\omega(t-(x\cos\varphi+y\sin\varphi)/c)} \\ &\times e^{-(\sigma_x\cos\varphi/\varepsilon_0 c)x} e^{-(\sigma_y\sin\varphi/\varepsilon_0 c)y}\end{aligned} \qquad [3.18]$$

$$Z = E_0 / H_0 = \sqrt{\mu_0 / \varepsilon_0} \,. \qquad [3.19]$$

The first part of the field component expression shows that the wave is propagating with the speed of light along the direction perpendicular to the electric field. The second part shows that the magnitude of the wave decreases exponentially along x and y direction. It is also evident that the impedance of the PML equals to that of vacuum, which means it is a "matched one".

Next we consider a wave transmission through PML-PML interface as is shown in Figure 3.24. It is assumed that the interface is infinite and perpendicular to x axis, and that both the incident and transmitted waves are plane waves. Since the ratio of the transmitted wave to the incident wave must be constant throughout the interface, for any two points A and B on the interface, one obtains :

$$\frac{\psi_t(B)}{\psi_i(B)} = \frac{\psi_t(A)}{\psi_i(A)} \,. \qquad [3.20]$$

When the two media are both "matched medium", i.e. both (σ_x, σ_x^*) and (σ_y, σ_y^*) satisfy the condition [3.15], then according to the field expression of Equation [3.18], one can derive the following relation from the above equation as:

$$(1 - i\frac{\sigma_{y1}}{\varepsilon_0\omega})\sin\theta_1 = (1 - i\frac{\sigma_{y2}}{\varepsilon_0\omega})\sin\theta_2 \,. \qquad [3.21]$$

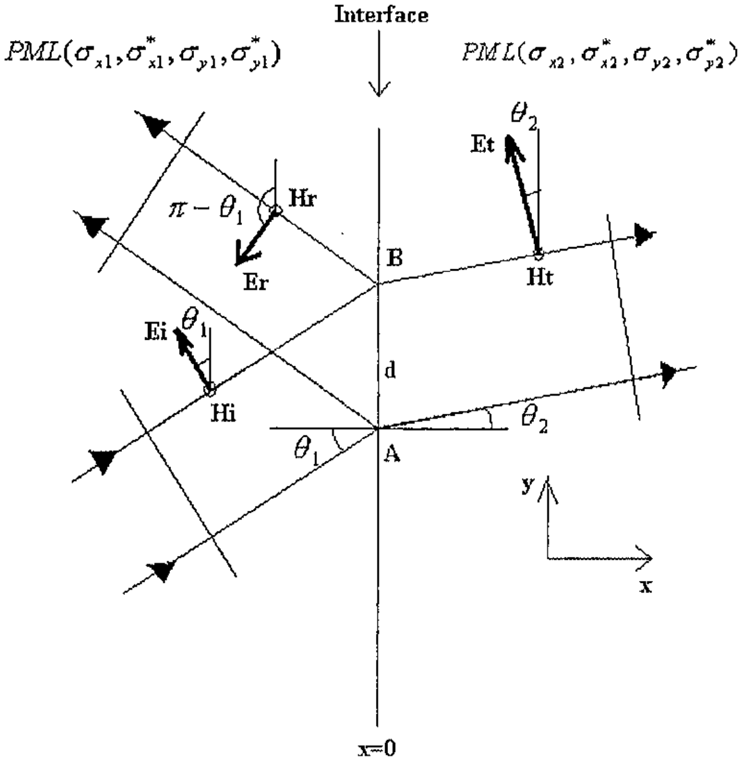

Figure 3.24 Interface lying between two PML media.

(Taken from Figure 2, Reference [46])

Since the field Ey and Hz must be continuous at the interface, we have

$$\begin{aligned} &E_i \cos\theta_1 - E_r \cos\theta_1 = E_t \cos\theta_2 \\ &H_i + H_r = H_t \end{aligned} . \qquad [3.22]$$

With the help of Equation [3.18] and [3.19], we can rewrite [3.22] as

$$\begin{aligned} &E_{i0} \cos\theta_1 - E_{r0} \cos\theta_1 = E_{t0} \cos\theta_2 \\ &\frac{E_{i0}}{Z} + \frac{E_{r0}}{Z} = \frac{E_{t0}}{Z} \end{aligned} . \qquad [3.23]$$

The reflection coefficient is the ratio of the electric components along the interface, i.e. $-E_{r0}\cos\theta_1 \,/\, E_{t0}\cos\theta_1$. According to equations [3.23], we can obtain the reflection coefficient as:

$$r_p = \frac{\cos\theta_2 - \cos\theta_1}{\cos\theta_2 + \cos\theta_1}. \qquad [3.24]$$

If these two media have the same σ_y and σ_y^* at the interface, Then Equation [3.21] reduces to

$$\theta_1 = \theta_2 \qquad [3.25]$$

and the reflection ratio becomes:

$$r_p = 0. \qquad [3.26]$$

In summary, if two matched PML media separated by an interface normal to the x axis have the same σ_y and σ_y^* at the interface, a plane wave can penetrate through the interface without any reflection quite independent and irrespective of the incident angle and frequency. For example, one PML could be a (σ_x, σ_x^*, 0, 0) medium and the other vacuum region can be treated as a (0 , 0 , 0 , 0) medium. This conclusion is also true for interface normal to the y axis when the two matched PML media have the same σ_x and σ_x^* at the interface.

In the numerical implementation, the actual formula used for the computer codes to update the field is given as:

$$\begin{aligned} Hzx^{(n+1/2)}(i,j) &= Hzx^{(n-1/2)}(i,j) \times e^{-\sigma^*\Delta t/\mu_0} \\ &\quad - (1 - e^{-\sigma^*\Delta t/\mu_0}) \times \frac{Ey^{(n)}(i+1,j) - Ey^{(n)}(i,j)}{\Delta x \cdot \sigma^*} \end{aligned}$$

$$
\begin{aligned}
Hzy^{(n+1/2)}(i,j) &= Hzy^{(n-1/2)}(i,j)\times e^{-\sigma^{*}\Delta t/\mu_0} \\
&\quad +(1-e^{-\sigma^{*}\Delta t/\mu_0})\times\frac{Ex^{(n)}(i+1,j)-Ex^{(n)}(i,j)}{\Delta y\cdot\sigma^{*}} \\
Ex^{(n+1)}(i,j) &= Ex^{(n)}(i,j)\times e^{-\sigma\Delta t/\varepsilon} \\
&\quad +(1-e^{-\sigma\Delta t/\varepsilon})\times\frac{Hzx^{(n+1/2)}(i,j)-Hzx^{(n+1/2)}(i,j-1)}{\Delta y\cdot\sigma} \\
&\quad +(1-e^{-\sigma\Delta t/\varepsilon})\times\frac{Hzy^{(n+1/2)}(i,j)-Hzy^{(n+1/2)}(i,j-1)}{\Delta y\cdot\sigma} \\
&\quad +(1-e^{-\sigma\Delta t/\varepsilon})\times Jx(i,j) \\
Ey^{(n+1)}(i,j) &= Ey^{(n)}(i,j)\times e^{-\sigma\Delta t/\varepsilon} \\
&\quad -(1-e^{-\sigma\Delta t/\varepsilon})\times\frac{Hzx^{(n+1/2)}(i,j)-Hzx^{(n+1/2)}(i-1,j)}{\Delta x\cdot\sigma} \\
&\quad -(1-e^{-\sigma\Delta t/\varepsilon})\times\frac{Hzy^{(n+1/2)}(i,j)-Hzy^{(n+1/2)}(i-1,j)}{\Delta x\cdot\sigma} \\
&\quad -(1-e^{-\sigma\Delta t/\varepsilon})\times Jy(i,j)
\end{aligned}
\qquad .\ [3.27]
$$

In this project, the general structure of PML boundary is set according to Figure 3.25. On the left and right sides, ($\sigma_x,\sigma_x^{*},0,0$) media are allocated. Thus, at the interface between the vacuum and the PML (CD and AB), the reflection ratio is zero according to what we have discussed above. Similarly, we allocate matched PML($0,0,\sigma_y,\sigma_y^{*}$) at the top and bottom sides so there is no reflection at the interface between the vacuum and the PML (AD and BC). At the four corners, PML ($\sigma_x,\sigma_x^{*},\sigma_y,\sigma_y^{*}$) is set to match both the ($\sigma_x,\sigma_x^{*},0,0$) and ($0,0,\sigma_y,\sigma_y^{*}$) media. By setting up this configuration of PML absorbing boundary, every electromagnetic wave propagates through the vacuum-PML interface will not suffer any reflection. Instead, in the absorbing layer, the penetrated wave magnitude will undergo an attenuation according to Equation [3.18]. And it is clear that this attenuation speed is the function of conductivity value σ as $e^{-\sigma\delta}$. Where δ is the absorbing layer's thickness.

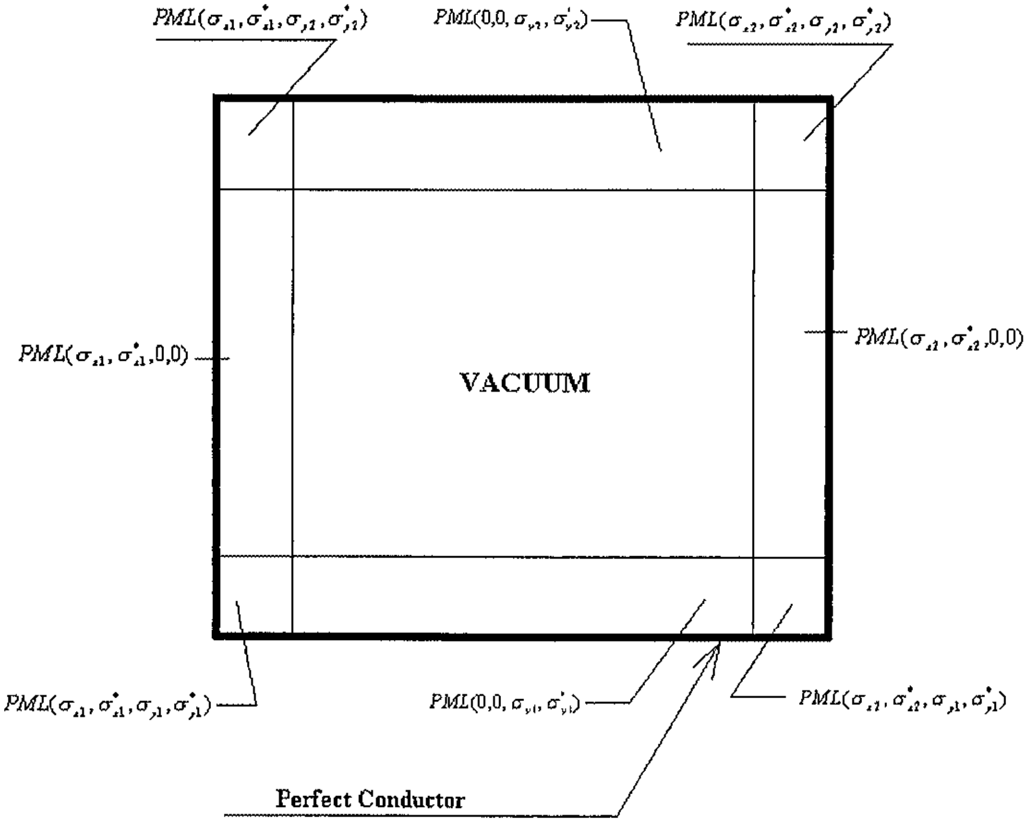

Figure 3.25 PML structure.

(Taken from Figure 3, Reference [46])

Since the penetrated wave will hit the perfectly conducting boundary and be reflected back into the vacuum region again, we want the attenuation inside the PML as large as possible. This requires very high conductivity value, but if we introduce very sharp change of conductivity between the vacuum and PML media, numerical reflection problems will arise. So in this project, we make the PML absorbing layer to be several cells thick, with a gradual increase of conductivity from zero value at the vacuum-PML boundary to a high value at the outer edge of the PML. The form of this increase is shown as

$$\sigma(\rho) = \sigma_m \left(\frac{\rho}{\delta}\right)^n . \qquad [3.28]$$

Where ρ is the distance from the vacuum-PML boundary. In this simulation case, n is set to be equal to 10.

3.4.3 Test Results for Full Maxwell Equations Simulation Method

The plots in this section show some results of a test on the full Maxwell equations simulation program. Figure 3.26 below shows the simulation condition.

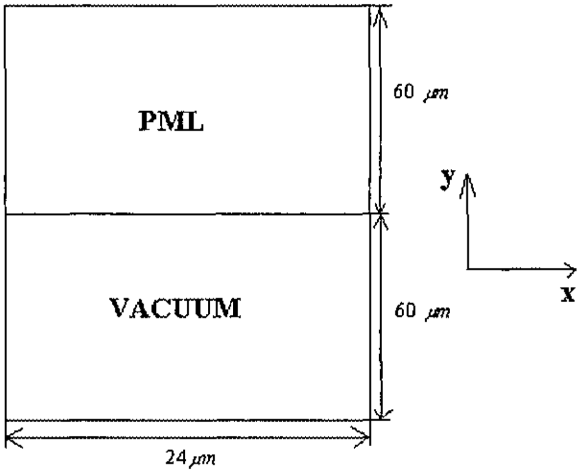

Figure 3.26 Simulation Structure.

From Figure 3.26, we can see that the whole simulation region is made up by a 24 μm x 60 μm vacuum region connected with a 24 μm x 60 μm PML region.

Figure 3.27 shows the initial electro-magnetic distribution. From this plot, we can see that the initial field is mainly concentrated on the vacuum region.

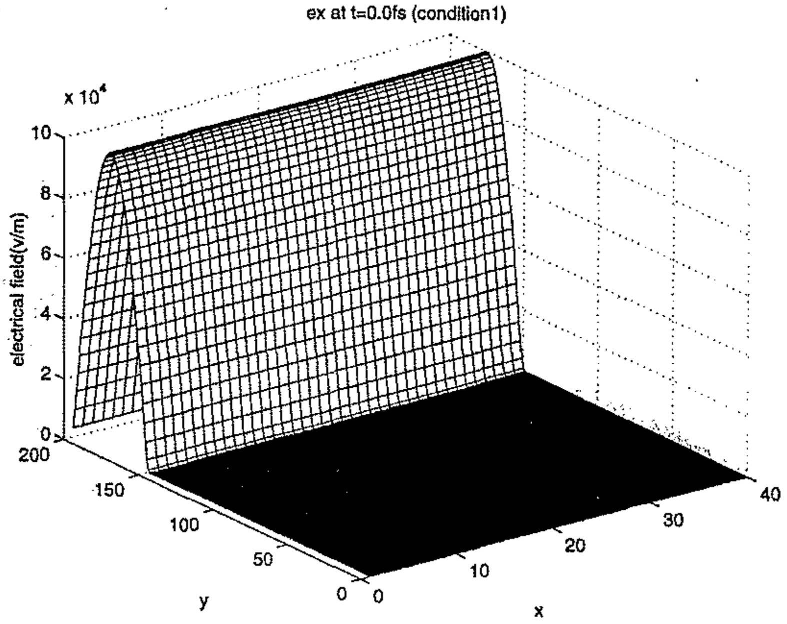

Figure 3.27 Initial electro-magnetic field distribution.

Figure 3.28~3.31 show the field propagation status at 100fs, 200fs, 300fs and 400fs. Figure 3.32 shows the time dependence of the field energy inside the vacuum. If we take a close look at these figures at the same time, we can get a very clear view of the field propagation in this case:

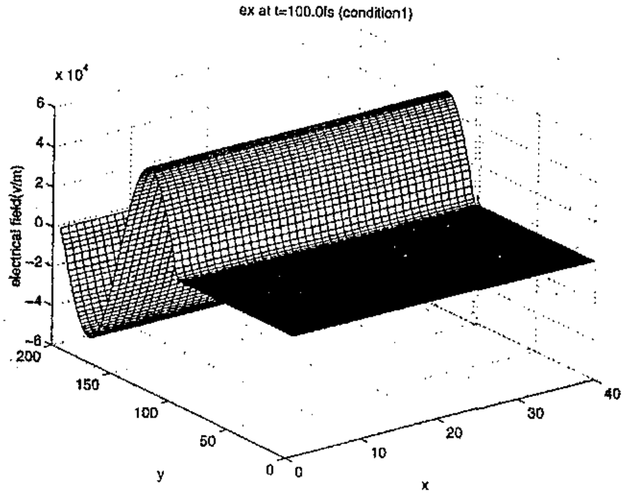

Figure 3.28 Electro-magnetic field propagation at t=100fs

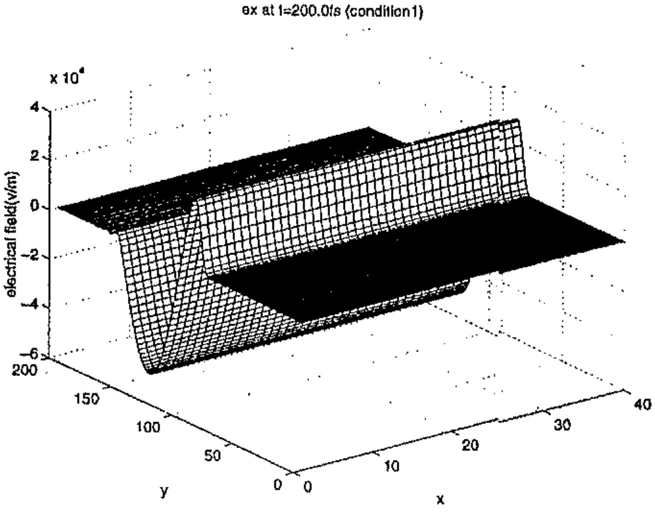

Figure 3.29 Electro-magnetic field propagation at t=200fs

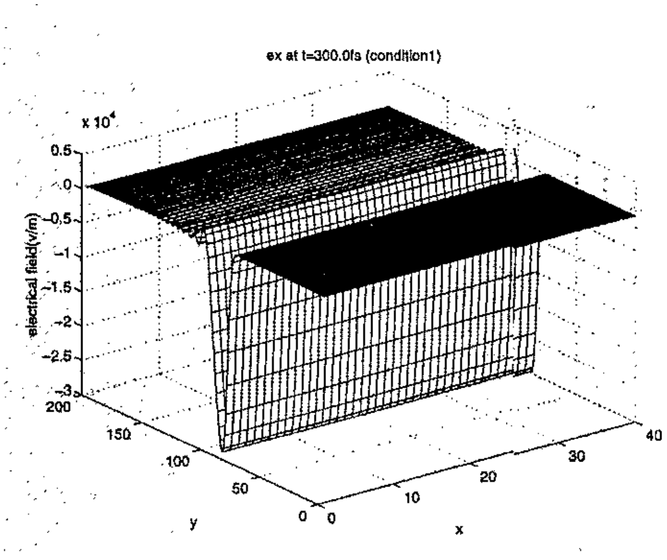

Figure 3.30 Electro-magnetic field propagation at t=300fs

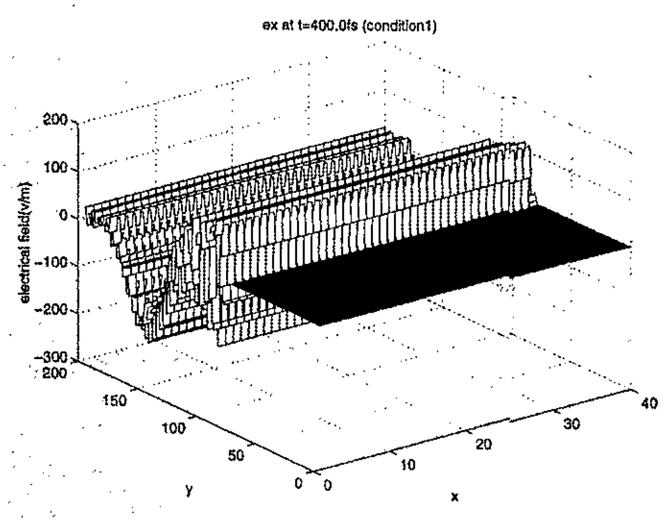

Figure 3.31 Electro-magnetic field propagation at t=400fs

First, this initial field splits into two parts going in the positive and negative direction along the y axis respectively. The part which goes along the positive direction hits on the vacuum-PML boundary after 100fs, which is exactly the field propagation time for this part ($t = L/c = \dfrac{30\mu m}{3.0\times10^{8}m/s} = 100fs$). Later, the other part will hit the vacuum-PML boundary at t=200fs, which also matches the propagation time ($t = L/c = \dfrac{60\mu m}{3.0\times10^{8}m/s} = 200fs$). From Figure3.32, we can see two drops of vacuum field energy corresponding to the events when one part of the field hits on the boundary and being absorbed later. This simulation result confirms the full absorption of the electromagnetic signal and validates our numerical implementation.

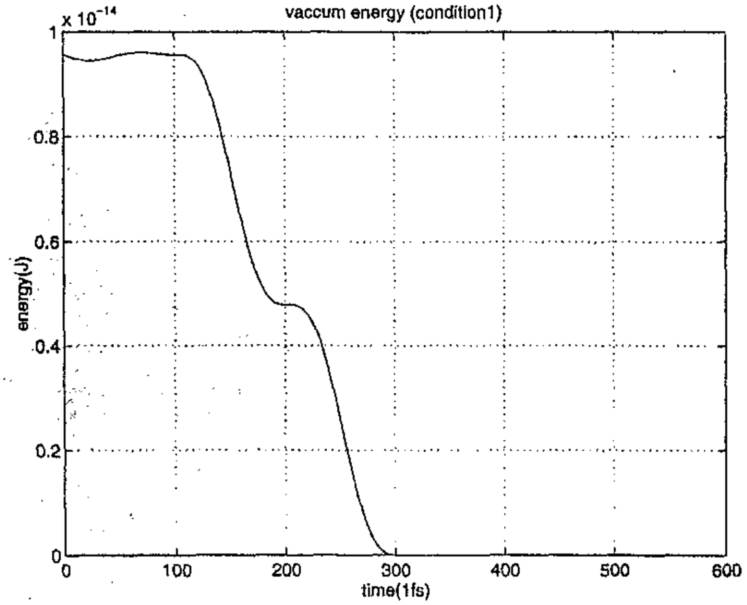

Figure 3.32 Vacuum field energy development.

CHAPTER IV

SIMULATION RESULTS

4.1 Introduction

In this chapter, we report on details of the simulation results obtained for the photomixing process. The techniques described in the previous chapter were used for the numerical calculations. The main goal of this work is to see how a photocurrent can be generated internally within the GaAs device at the difference frequency of the two input lasers. In particular, the dependence of such a photocurrent on various parameters such as the input laser signal intensity, the operating voltage, the optical wavelength, and the effect of LTG material on the mixing process, will be evaluated quantitatively. In the end, we have simulated the photomixing process for different conditions by varying the laser injection power, frequency difference, photon energy or the electric field intensity. The results and output trends are also discussed in this chapter.

4.2 Device Structure for Simulation

The simulation geometry is shown in Figure 4.1. This simulation structure consists of a uniform PML(perfectly matched layer) which completely surrounds the vacuum region and the MSM simulation box is located right in the center.

For the sake of symmetry, two $V_A / 2$ batteries in series have been used to provide a total bias of V_A volts across the MSM device. For purposes of numerical evaluation, the entire simulation region was divided into a uniform three-dimensional mesh with a grid spacing of 5nm. The top surface was taken to coincide with the x-z plane for reference, and its y value is set to be zero. Two electrodes, each 50nm wide, were assumed to be on the surface of the GaAs material separated by a 150nm distance. Along the y and z axes, the device thickness was taken to be 100nm and 2.5 μm, respectively. These dimensions are typical of actual devices currently being fabricated and tested at NASA, Langley. The vacuum region was taken to surround the semiconductor device completely, with its dimension along the three x-, y-, and z-axes being 250nm, 300nm and 2.5 μm, respectively. Similarly, the PML region surrounding the vacuum had dimensions of 500nm, 500nm, 2.5 μm.

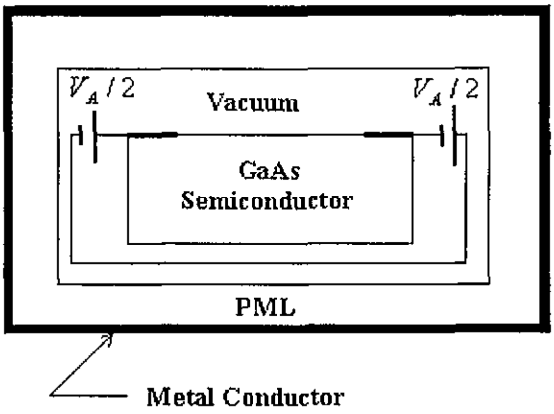

Figure 4.1 Schematic of the simulation geometry used.

4.3 Results for Static Cases

The ultimate objective of this thesis is to get some numerical predictions of both the photocurrent produced at the difference frequency between the two input lasers, and the terahertz radiation generated by the optical-mixer device. Hence, in general, joint application of the EMC with the full Maxwell equations simulation method is necessary. In the absence of time dependent fields, aspects that related to radiation from the GaAs device as well as internal polarization effects could not be adequately incorporated. However, it has been observed and is also expected, that the photocurrent is not very sensitive to the dynamic variations of the fields, at low levels of input laser power. Hence, the shape and magnitude of the photocurrent are not dramatically affected by assuming a static, time invariant fields if the induced laser power is roughly below 50mW. Thus, it is perhaps reasonable to first carry out a few test simulations without updating the electro-magnetic fields. Although such test cases would not yield any information about the terahertz, at least it is expected to give reasonably accurate information about quantities such as the photocurrent, internal power dissipation, conversion efficiency, carrier energy and its temporal behavior, carrier velocity distribution, and so on. Besides, the speed of the simulations would be enhanced significantly, since a lot of computational time is saved for not updating the fields.

4.3.1 Initial Steady-State Field Results

The initial field is calculated by the full Maxwell equation method. We first set the initial field within the whole simulation region (including the semiconductor, vacuum and PML) to be zero, except for the field inside of the battery. After about 2ps propagation of the fields in time according to Maxwell equations, it showed that the field distributions in space and time stabilized towards an invarient state. As the magnitude and shape of the fields stayed fixed after the 2ps simulation time, these field distributions were taken to accurately describe the initial electric field profile for the static simulation case.

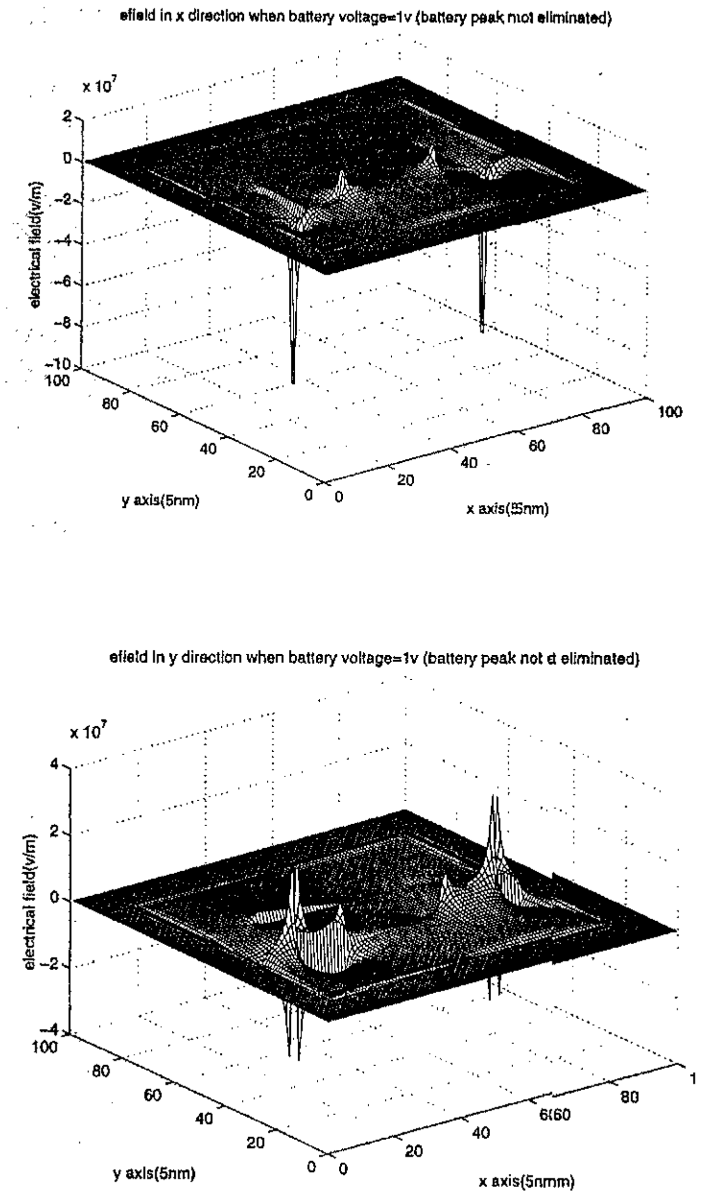

efield in x direction when battery voltage=1v (battery peak mot eliminated)

efleld In y direction when battery voltage=1v (battery peak not d eliminated)

Figure 4.2a Initial electric field with battery field peak.

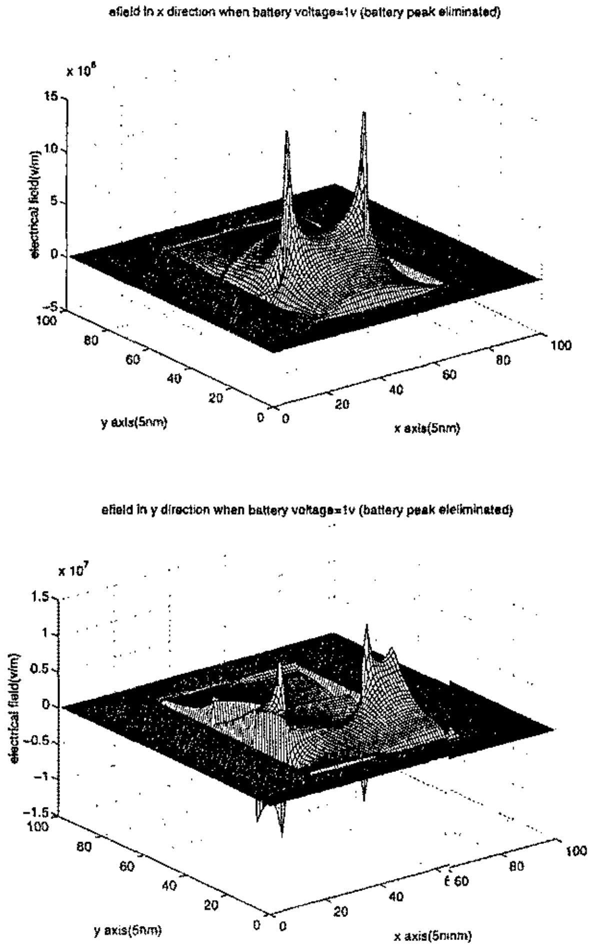

efield in x direction when battery voltage=1v (battery peak eliminated)

efield in y direction when battery voltage=1v (battery peak eleliminated)

Figure 4.2b Initial electric field with battery field peak eliminated.

Figure 4.2a shows the initial field before the photoexcitation process, while Figure 4.2b shows the field distribution obtained by omitting the battery peak electric field. As can be expected, the field has very high values at the electrodes and near their edges. The peak value, however, is lower than the reported breakdown field of LTG GaAs material. Hence, application of a 1.0 Volt bias is quite appropriate for the chosen device structure and geometry.

4.3.2 Case I (Zero Field Test With Laser Input With LTG – GaAs Material)

As an initial test of the external photoexcitation on the LTG-GaAs device, a zero field static simulation was carried out. A zero field was deliberately used, since one expects the circuit currents to be zero. This knowledge and expectation of the current output, enables one to compare the results of the simulation for validation purposes. The simulation conditions chosen are shown in Table 1.

Laser power	1mw
Laser frequency difference	1THz
Laser photon energy	1.55ev
Battery voltage	0v
Recombination time constant	0.25ps

Table 1 Simulation conditions for case I.

As given in Table 1, the LTG-GaAs material with a very short recombination time of 250 fs was chosen. This value is among the smallest reported values in experiments. Hence, the fastest carrier response is to be expected.

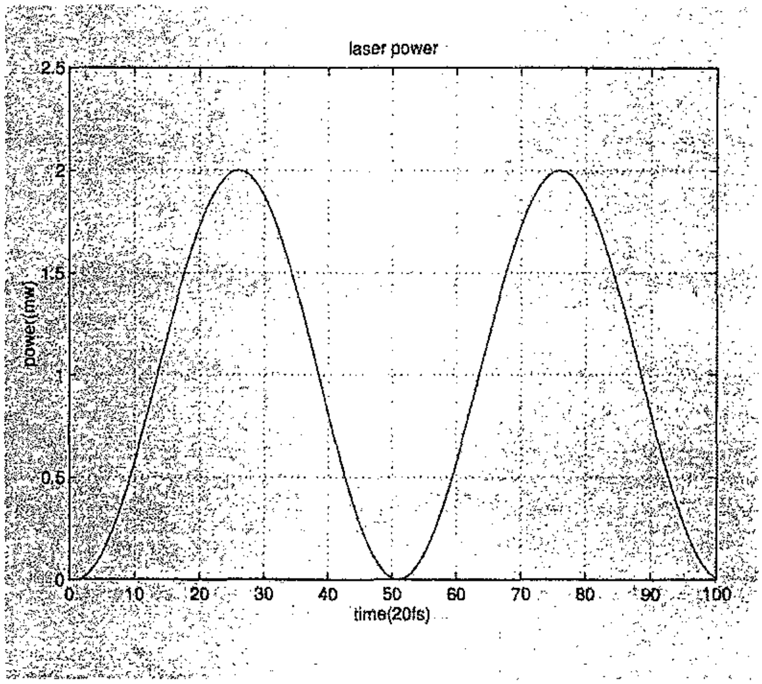

Figure 4.3 Input laser power in case I.

Figure 4.3 shows the input laser power oscillating at a frequency of 1THz with an average power of 1mW. Figure 4.4 shows the simulation result for the energy development inside the semiconductor. The electron and hole energies shown correspond to the mean carrier energies beyond the band edges. These two energies are seen to oscillate roughly at the same frequency as the external laser input. This is the direct result of the fast trapping and carrier recombination effects of the LTG GaAs material. The fast trapping effect quickly removes the photogenerated carriers, thus making the device respond quickly to such high frequency optical carrier injection. The electrode, phonon, and trap energies denote the energies being absorbed by the metallic electrodes, the phonons in the semiconductor, and the traps, respectively. Physically, this collective energy is supplied by the laser and the battery which function as the two inputs to the system. Hence, based on the general energy balance, the battery energy can be calculated as:

battery energy = electron energy + hole energy + phonon energy

+ trap energy + electrode energy - laser energy.

Since battery voltage is zero in this particular case, the field is zero everywhere. Hence, for this test case, one can say for sure that the battery cannot contribute any energy into the system. All the energies, such as electron, hole, phonon, trap, and electrode, must therefore arise from the input laser energy. This is validated from the numerical results shown in Figure 4.5. It is seen that the battery energy is zero, except for some insignificant numerical oscillations.

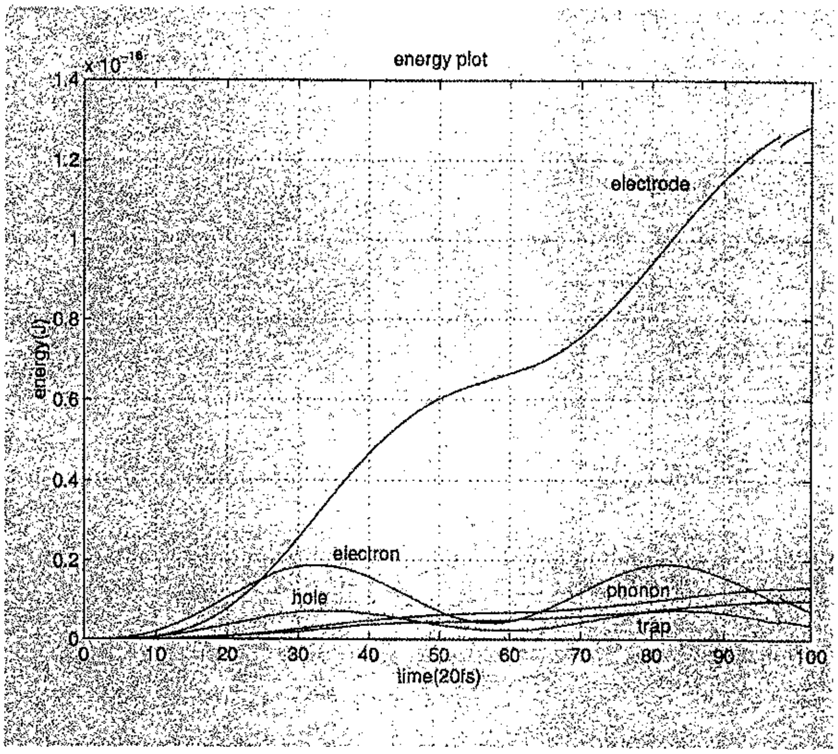

Figure 4.4 Energy development in case I.

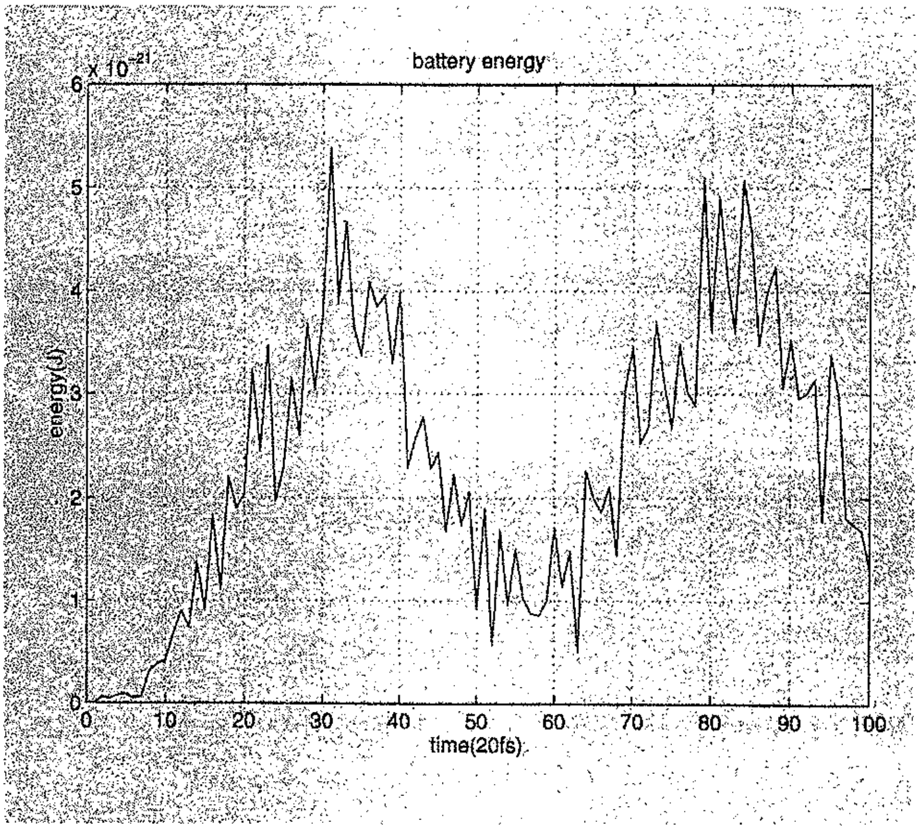

Figure 4.5 Energy provided by battery in case I.

4.3.3 Case II (Laser Dependent LTG Simulation With External Field)

In this simulation, an external 1.0 Volt bias was applied. Hence, an electric field was taken to exist within the semiconductor. The initial electro-magnetic field, which is calculated under the 1.0 Volt battery condition and discussed in section 4.3.1, was used. The magnitude and distribution of this initial field were the same as those already shown in Figure 4.2. The other conditions are shown in Table 2.

Laser power	1mw
Laser frequency difference	1THz
Laser photon energy	1.55ev
Battery voltage	1v
Recombination time constant	0.25ps

Table 2 Simulation conditions for case II.

Figure 4.6 shows that various energy developments inside the semiconductor in this case. The electron and hole kinetic energies oscillate roughly with the laser difference frequency. The electrode, phonon, and trap energies also increase as in the former zero field case. The only difference is that for this case, energy is being supplied by both the laser and the external battery since the electric field is now non-zero. According to the energy balance calculation method, one can now obtain the battery energy as:

battery energy = electron energy + hole energy + phonon energy
+ trap energy + electrode energy - laser energy.

The battery energy obtained from the simulation as a function of time from the above formula is shown in Figure 4.7. This figure demonstrates that the battery provides energy to the system in a time dependent manner, and oscillates at the laser difference frequency. By differentiating the battery energy with time, we get the battery power, then the photocurrent can be calculated by dividing the battery power by the battery voltage. Figure 4.8 shows the temporal development of the photocurrent. From this plot, one can observe that the average photocurrent produced by the dual laser inputs is about 0.15 mA for this case.

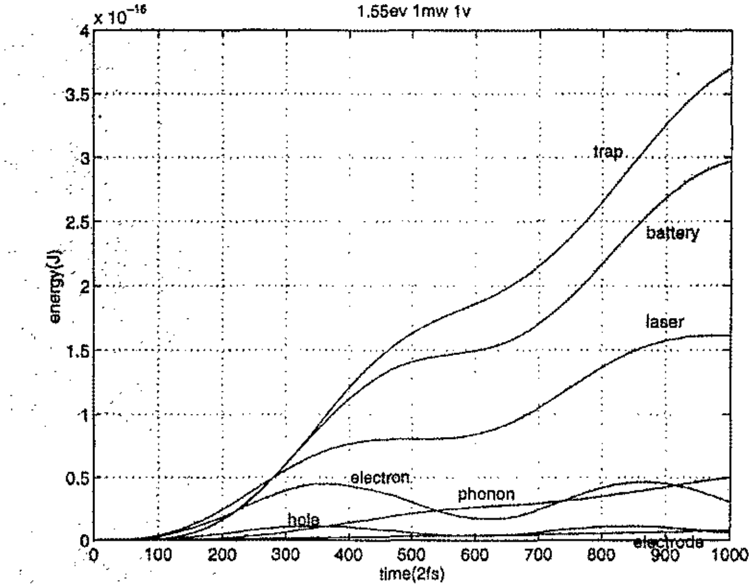

Figure 4.6 Various energy development in case II.

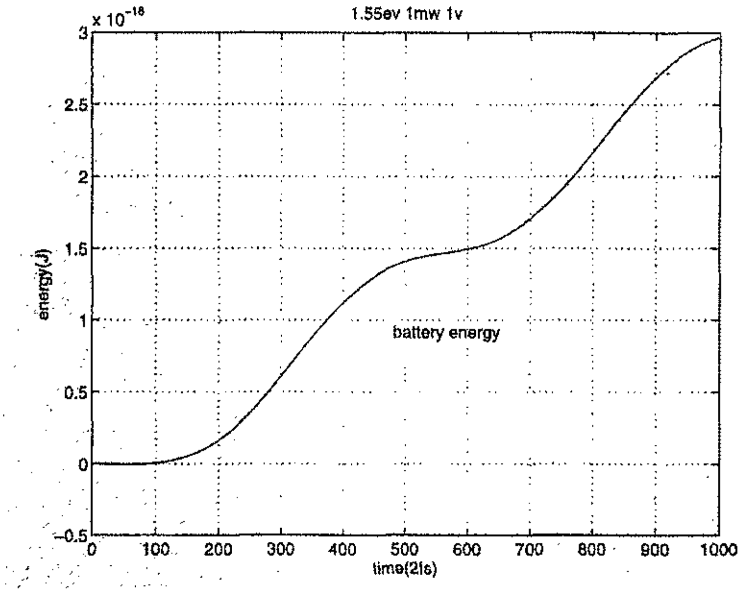

Figure 4.7 Energy provided by battery in case II.

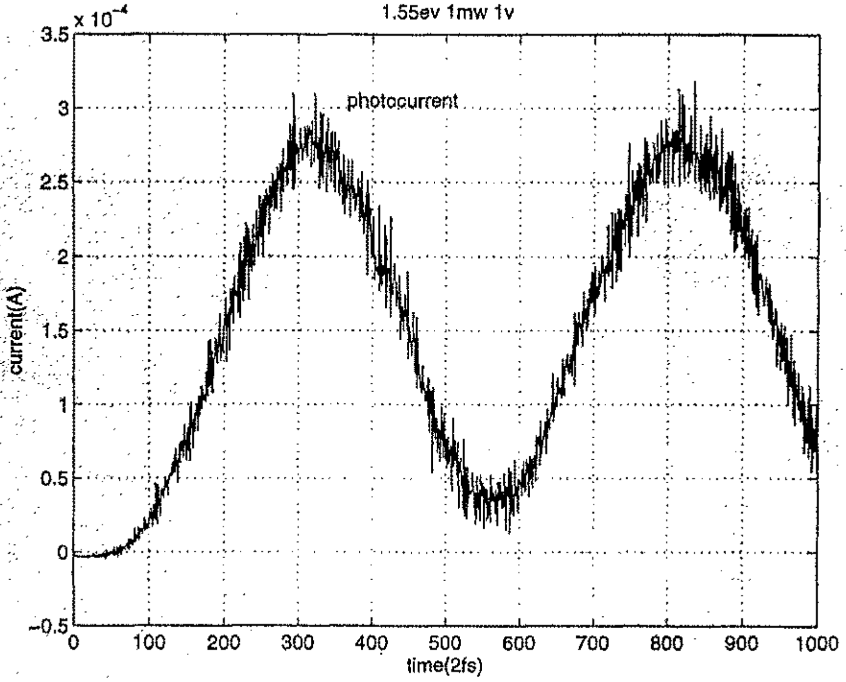

Figure 4.8 Temporal development of photocurrent in case II.

4.3.4 Case III (Various Other Simulations For LT-GaAs Material)

A particular set of parameters for the geometry, biasing condition, laser input wavelength, and recombination time constant was used in the simulations given in the above section. However, as the output current depends on several parameters, it becomes necessary to systematically evaluate the role of each parameter in optimizing the photocurrent response. Hence, several simulations were carried out, each with some variations of the input parameters, to probe their affects on the output. Thus, several simulation cases were analyzed with different values of the laser photon energy, the battery voltage, and the material recombination time constant. Table 3 and Figure 4.9 show the calculated photocurrent values of some of these cases.

	Battery Voltage=0.5v	Battery Voltage=0.8v	Battery Voltage=1.0v
Photon Energy=1.55ev	9.50e-5A	1.43e-4A	1.60e-4A
Photon Energy=1.97ev	3.51e-5A	6.78e-5A	7.23e-5A

Table 3 Photocurrent of LTG material at different static cases.

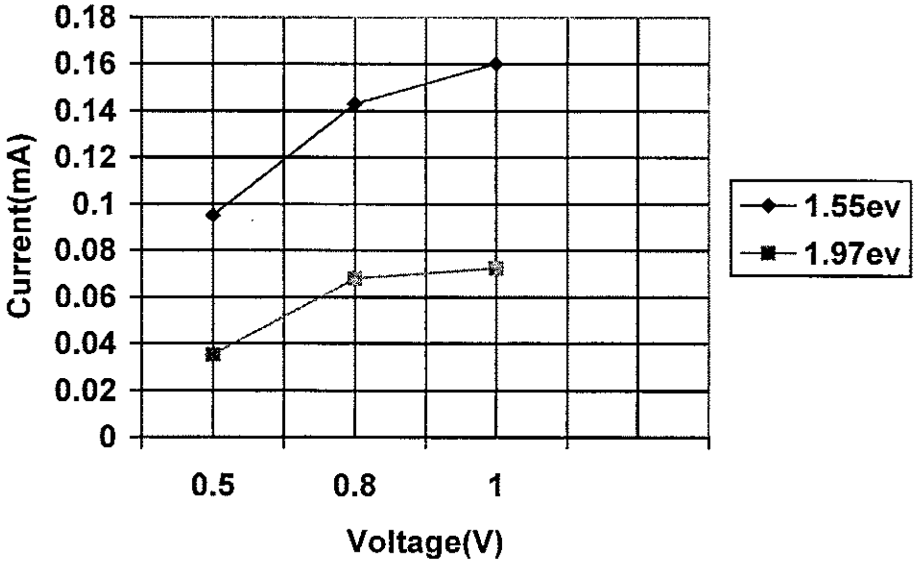

Figure 4.9 Photocurrent of LTG material at different static cases.

4.3.5 Case IV (Simulations For Non-LTG Material)

We also did some simulations on Non-LTG material, which has much longer recombination time. For the sake of convenience, we shut off the recombination effect in this case. The rest simulation condition is the same as case II. Because no recombination effect means higher carrier density inside the device, the photocurrent is expected to be higher. Figure 4.10 shows the photocurrent development in this case with a mean value of about 0.23 mA, which is higher than that in case II. In case II, the photocurrent oscillates approximately between 0mA and 0.3mA, while it oscillates between 0.15mA and 0.40mA in case IV. The simulation also shows that if we only change the photon energy from 1.55ev to 1.97ev, the photocurrent value will drop to 0.15mA, which is higher than that in the same condition for LTG material.

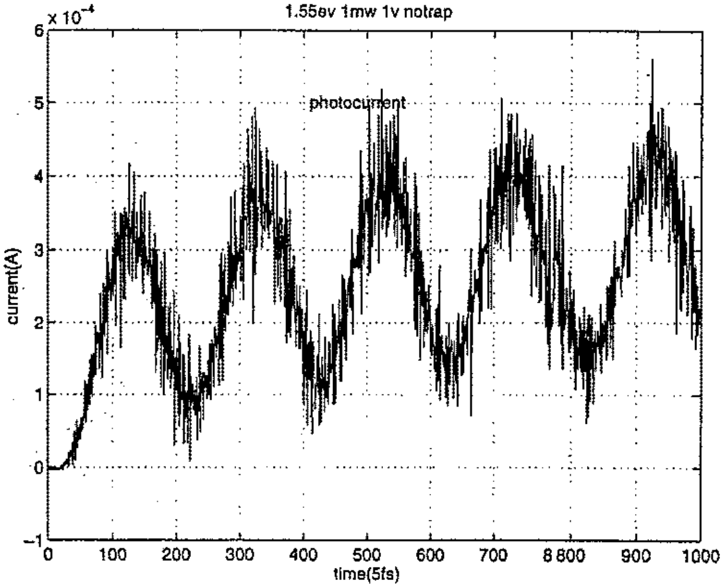

Figure 4.10 Photocurrent development in case IV.

	Battery Voltage=1.0v
Photon Energy=1.55ev	0.23mA
Photon Energy=1.97ev	0.15mA

Table 4 Photocurrent of non-LTG material at different static cases.

4.4 Results for Dynamic Cases

In the previous sections, the simulation results for the photocurrent were obtained for the static cases under several conditions. A low input laser power was assumed to keep high density effects such as internal space-charge polarization to a minimum. The results obtained were shown to be quite reasonable, and compared well with the available experimental data under similar conditions. Hence, the simulations effectively demonstrated the validity of the EMC numerical scheme and its successful implementation. As a further refinement in the model, the full Maxwell equations are now coupled with the EMC technique. This allows the calculation of dynamic fields, the prediction of input power dependent space charge effects, and the quantitative evaluation of the radiations from the photomixer system. Dynamic calculations, which include the Maxwell equations, are important for the high frequency domain modeling for the following reasons. First, in the THz regime, the characteristic carrier relaxation time scales begin to approach the period of the propagating electromagnetic waves. One can then no longer separate the electromagnetic phenomena as being quasi-stationary relative to the internal carrier processes. Instead, it becomes very important to incorporate all dynamic interplays between the propagating electric fields and their influence on carrier transport through continuous adjustments of carrier velocities. Second, the standard approach of evaluating internal electric fields through Poisson's equation is inappropriate since it ignores the propagation aspect, disregards the presence of the vector potential, and discounts the Lorentz force contributions to carrier motion. A general and complete treatment of the terahertz photomixer problem, therefore, requires inclusion of the dynamic mutual interactions of a propagating wave with the photogenerated carriers.

4.4.1 Initial Field

Just as in the static case, the initial field is calculated by the full Maxwell equations method.

4.4.2 Case I

Let us now discuss one dynamic case of simulation. The simulation condition is shown in Table 5 below:

Laser power	1mw
Laser frequency difference	1THz
Laser photon energy	1.55ev
Battery voltage	1v
Recombination.	No such effect

Table 5 Simulation conditions for case I.

Figure 4.11 shows that various energy developments inside the semiconductor in this case. The electron and hole kinetic energies oscillate roughly with the laser difference frequency while the electrode, phonon, and trap energies will increase as the static case II. The only difference is that for this case, field energy also changes. According to the energy balance calculation method, one now obtains the battery energy as:

battery energy = electron energy + hole energy + phonon energy

+ trap energy + electrode energy + field energy- laser energy.

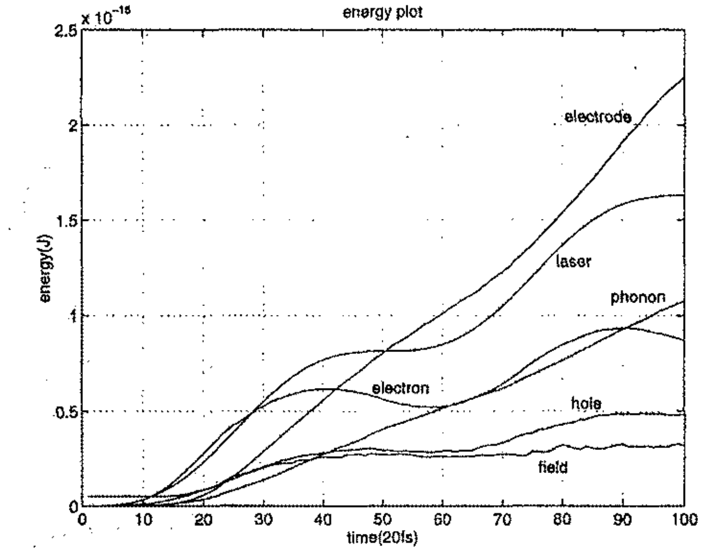

Figure 4.11 Various energy development in case I.

The battery energy obtained from the above formula is shown in Figure 4.12. Figure 4.13 shows the temporal development of the photocurrent. From this plot, one can observe that the average photocurrent produced by the dual laser inputs is about 0.15 mA for this case, which is less than that in the static case.

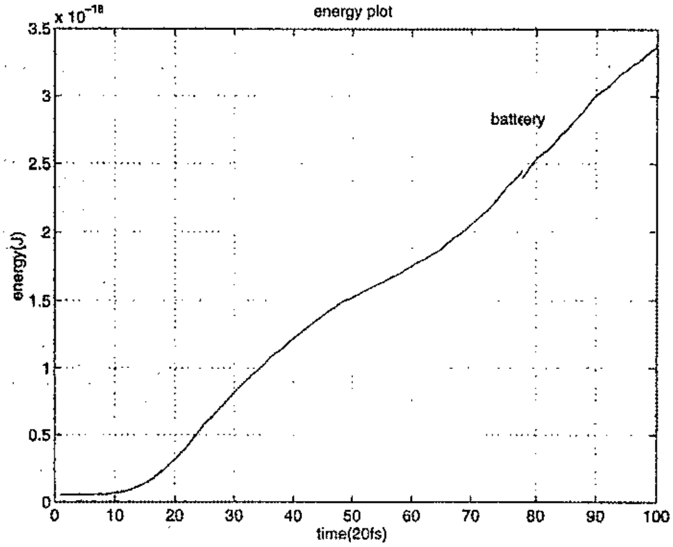

Figure 4.12 Energy provided by battery in case I.

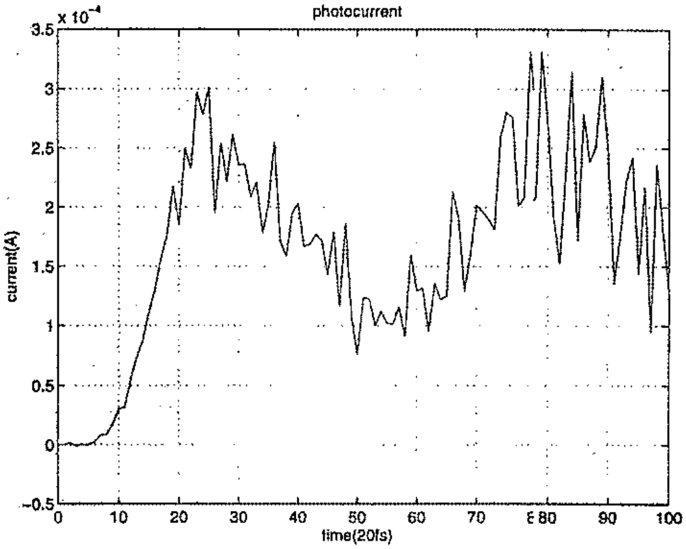

Figure 4.13 Photocurrent in case I.

The most significant advantage of the dynamic simulation is that it can provide the information of radiation. In this case, we have recorded the $E \times H$ value along the surface of the semiconductor, and the recorded radiation power is shown in Figure 4.14.

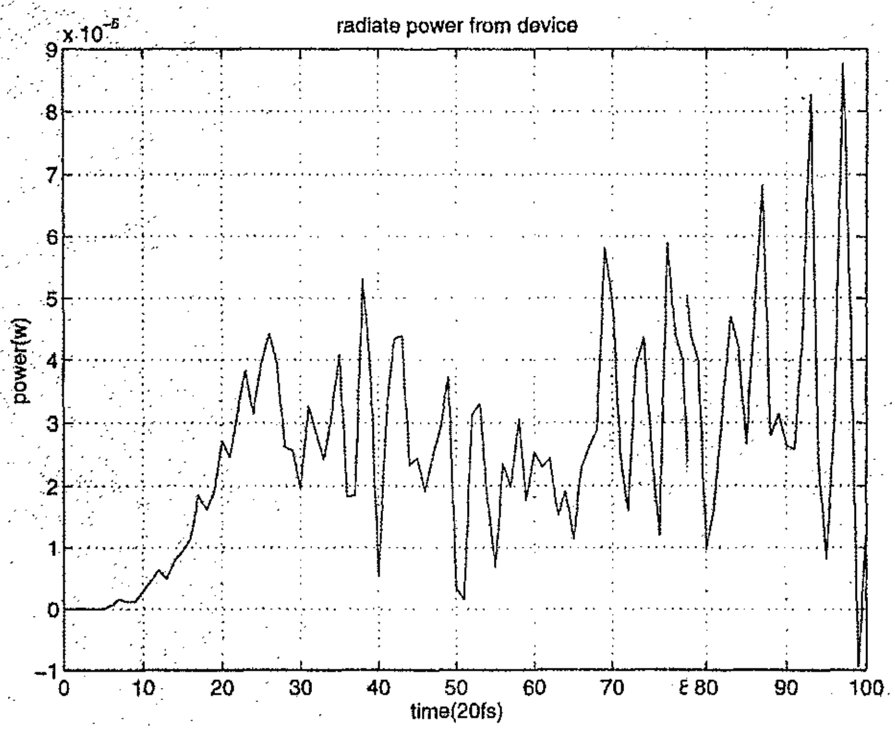

Figure 4.14 Radiation power from semiconductor.

4.4.3 Case II (Various Other Simulations)

We also have done several other simulations with the same condition as in case I except the different photon energy or laser power, the result is shown in table 5 and Figure 4.15.

	Laser Power=1mw	Laser Power=5mw	Laser Power=10mw
Photon Energy=1.55ev	2.0e-4A	2.4e-4A	3.0e-3A
Photon Energy=1.97ev	1.5e-4A	1.7e-4A	2.1e-3A

Table 6 Photocurrent of non-LTG material at different dynamic cases.

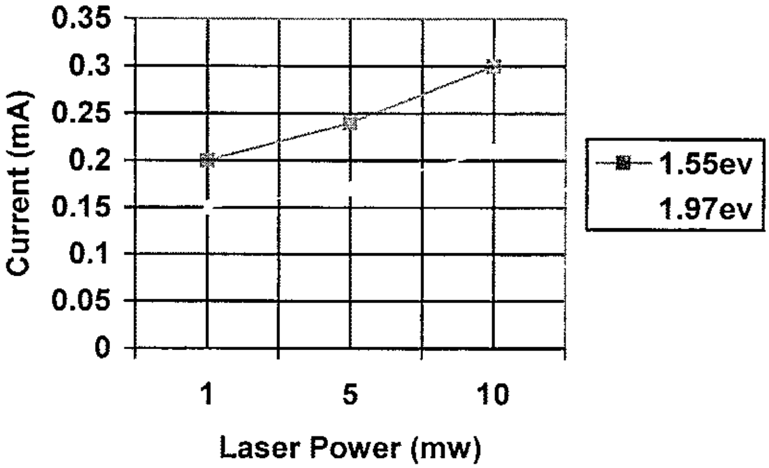

Figure 4.15 Photocurrent of non-LTG material at different dynamic cases.

4.5 Comparison with Experimental Data

It is always important to compare the simulation predictions with the available experimental results, since this is the only way to check for the accuracy and correctness of the result obtained.

Although a lot of experimental work has been carried out in this area of optical mixers, but most of the studies only provide reports of the output power radiated from an overall antenna system. The use of a variety of antenna systems has been discussed. However, specific data for the device photocurrent neither has been widely reported nor has been discussed. Up until now, we have found only a single experimental data result on device photocurrent from a report by E.R. Brown et al. [26]. This group is at MIT, Lincoln Laboratories and has been pioneering the experimental efforts. Some experimental results on a LTG-GaAs material (with a 0.2ps recombination time), which has an interdigitated-electrode geometry, were described. Their photomixer consisted of twenty 0.4-μm-wide electrodes separated by 0.6 μm gaps, and was pumped by two modes of a solid state $Ti:Al_2O_3$ laser operating at a wavelength near 750nm ($h\nu = 1.65eV$). This operating photon energy is thus slightly higher than the 1.55 eV case simulated here.

However, most of our simulation work in this thesis research, has been done for a GaAs device having a 250nm gap and 1.0 Volt biasing. Our dimensions were deliberately smaller, since better performance is expected with decrease in device dimensions. Hence, a direct head-to-head comparison is impossible with the experimental data. Nonetheless, one could seek a crude comparison by choosing to look at the experimental data that has the same average internal electric field. This implies to choose an operating condition from the experimental data that has the same voltage/air gap ratio. For the devices dimensions of Reference 26, this translates into an applied bias of 2.4 Volts. In Figure 4.16, we show the photocurrent values calculated by the current simulations for our chosen devices, and that detected from experiments [26] at 2.4 V bias, for different laser pump powers.

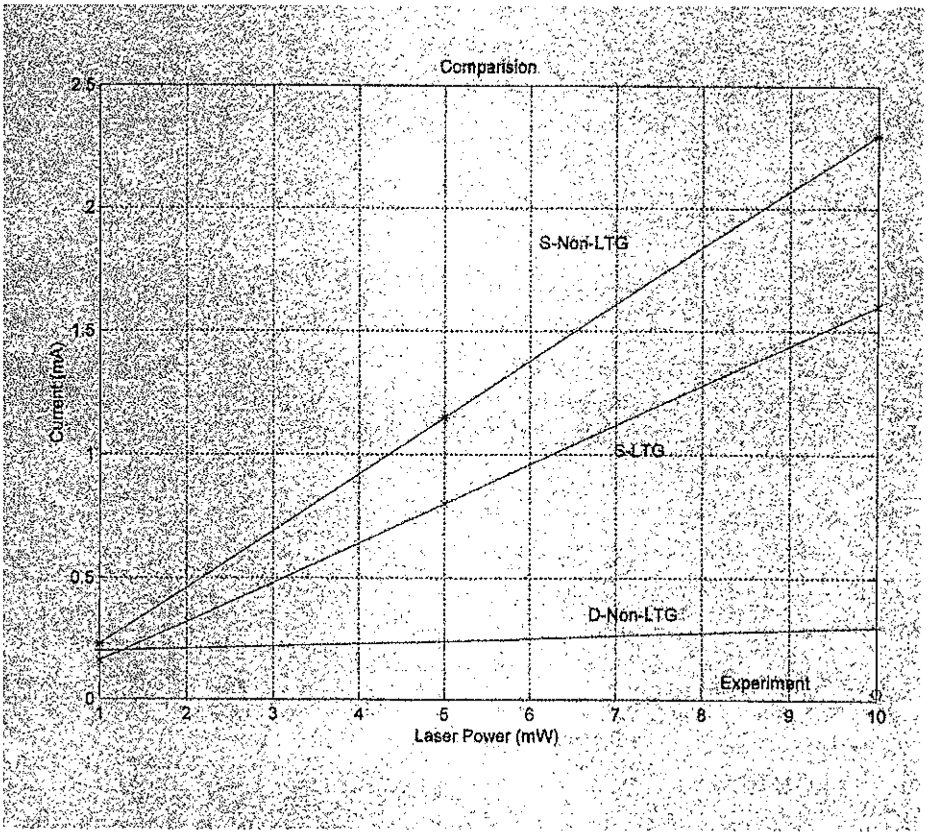

Figure 4.16 Comparison simulation results with experimental results.

In figure 4.16, S-LTG indicates simulation results on LTG material for the static case, S-Non-LTG denotes trap free material under the static case, while the D-Non-LTG curve represents results for the trap free material under dynamic conditions. Although all the static case simulations shown in this chapter were for the 1 mW case, the photocurrent was seen to scale directly with the laser pump power. Hence, the results shown in Fig. 4.16 at different pump powers were obtained by simply scaling the 1mW pump power data. This linear scaling under static conditions occurs because the carriers are assumed not to take any effect on the electro-magnetic field. As a result, irrespective of the number of photoexcited carriers in this device, the entire density moves under the same time-invariant electro-magnetic field. This static field assumption is clearly unphysical and cannot be expected to yield accurate results. As the laser injection power increases, one expects a larger decrease in the internal fields due to the polarization effects. Hence, linear enhancements, as predicted by the static model, would over-estimate the photocurrents. The dynamic case simulations, on the other hand, correctly build in the non-linear density dependent polarization effects, and hence should yield more accurate results at all power levels.

This is indeed evident from Figure 4.16. The dynamic calculations are much closer to the available data point. However, the current predicted at 10 mW is of about 0.35 mA, as compared to 0.03 mA for the experiments. This higher value can be attributed to the difference in materials. The experiments were conducted on LTG GaAs with a 0.2 ps recombination time, while the D-Non-LTG simulations were done on trap free material. As a result, not all of the 1.66 eV photon energy is converted into useful electric energy for the LTG material. Crudely speaking, only 0.25 eV, which is the difference between the incident energy and the bandgap (1.66 eV – 1.41 eV), effectively contributes to the electric energy. Hence, for Non-LTG material, one would roughly expect a photocurrent enhancement by a factor of about 1.66/0.25 = 6.65. As a result, for a fair comparison between our dynamic, non-LTG results and the experimental data, the photocurrents should be taken as: 0.35 mA and 0.2 mA, respectively. These values with the effective correction, are reasonably close and denote a good agreement between the experiment and theory.

CHAPTER V

CONCLUSION

5.1 Conclusion Summary

A theoretical model based on a coupled Electrodynamic-Monte Carlo scheme has been developed for analyzing the performance of nanoscale GaAs terahertz optical mixers. This model was implemented into a suitable numerical code and successfully tested. The effects of different parameters such as pump laser photon energy, applied bias, device size, and pump power have been discussed. All the internal microscopic details of carrier transports under the high frequency input signal conditions have been built into the simulation. Based on the numerical model developed here, simulations were carried out to analyze and predict the electric response of optical photomixers. The aim was on the study of small device dimensions for possible performance and efficiency enhancements. The role and effect of various parameters such as the laser pump energy, the applied bias, device size and excitation wavelength have been examined. Numerous results for both the static and dynamic cases on LTG and trap free GaAs material have been given, and compare with the current experimental results.

5.1.1 Summary on LTG Material Simulation at Static Case

From the simulation results obtained for the static case, the dc photocurrent values were seen to increase with the applied biasing. This result is to be expected, since the carrier velocities, and hence the currents, are enhanced at higher electric fields. This can also be viewed in terms of larger energy delivery into the system by the battery at higher bias. Thus, it helps drive a higher current output. Also the results show that the photocurrent is larger at the smaller photon energy. The two photon energies (i.e. wavelengths) chosen correspond to photogeneration close to the conduction band edge and above the intervalley transfer threshold. The simulation results indicate that higher wavelength excitation near the band edge should be considered favorable for this photomixer system. Physically, this decrease of the current with photon energy arises from the bandstructure of GaAs material. At high photon energies, the electrons are created within states high in the central Gamma-valley. These carriers have large kinetic energies exceeding the threshold for transition into the satellite L and X valleys. As a result, these electrons can immediately scatter into the neighboring satellite valleys. This scattering mechanisms reduces the mobility by increasing the energy loss and momentum randomization processes. Furthermore, once the electrons transfer into the satellite valleys, their effective mass increases. This also contributes to a more sluggish movement. The overall result is that the electron flow becomes slower as the excitation energy becomes higher. Similarly, the holes are also slowed down by the higher energy photogeneration. At higher energies, the holes acquire enough energy to scatter among the heavy, light and spin-split-off bands. This enhancement in the collision frequency reduces the hole mobility. Furthermore, since the scattering rates increase with energy, which is shown in the previous chapter, the mobility decrease is expected to become more significant with higher photon energies. Therefore, photomixer systems would yield optimal performance if they are operated close to the band edge.

5.1.2 Summary on Non-LTG Material Simulations at Static Case

The analysis for non LTG-GaAs (i.e. trap free material) reveals that the photomixer can essentially produce a higher DC photocurrent component. This can be easily understood because the non LTG-GaAs material does not have any strong trap effect. As a result, the density of photogenerated carriers inside this material is higher when compared to that in the LTG-GaAs material under the same conditions. However, the photocurrent for the non LTG-GaAs material displayed smaller oscillation amplitude, which means a worse frequency response capability. Physically, this occurred because the photoexcited carriers could only survive inside the LTG material for very short times (less than 1.0 ps), and were subsequently absorbed by the trap. LTG material could therefore, respond more quickly for ultra-fast frequencies. But if the trap effect is not so strong in the non-LTG material, the photogenerated carriers can not be absorbed quickly. This reduces the frequency response capability. Also, from the simulation results on non-LTG–GaAs, the heat problem is predicted to be less severe than that with the LTG materials.

5.1.3 Summary on Non-LTG Material Simulation at Dynamic Case

From the results shown previously, the photocurrent has been predicted to increase with the input laser power. This trend agrees with the physics and experiments. However, the extent of this increase differs significantly between the static and dynamic cases. In the static case, carrier movement does not have any effect on the internal electro-magnetic fields. So, no matter how high the laser power is, the photogenerated carriers always undergo the same time-invariant fields. Hence, the calculation on simulated photocurrent at different values of the laser input power becomes a simple scaling problem. At low laser pump levels, this simulation gives reasonable results. But at high pump levels, the difference between simulation and experiments cannot satisfy our requirement. This was shown through a careful comparison between the simulation result and the available experimental data.

Unlike the assumption made under static field conditions, the photocurrent does not increase linearly with the laser power due to the polarization effect of the carrier movement on the electro-magnetic fields. From a comparison between the simulation result and experiment data, the dynamic case simulation has been shown to give more reasonable results than the static case does, especially at high laser pump condition. It was also shown that under the same condition, the 1.97ev photon excitation (i.e. lower wavelength) generates less photocurrent than the 1.55ev photon excitation does. This has already been explained in section 5.1.1.

5.2 Suggestions for Future Work

Work has been done for non-LTG GaAs devices under both static and dynamic field conditions in this thesis. However, only LTG GaAs devices under static conditions were analyzed. Since the dynamic case has been shown to yield more reasonable results, it is obvious that more work on the dynamic case for LTG GaAs needs to be carried out. The practical problem is that large computational time is required to simulate the trapping process and its effects.

Some of the other issues and areas that could be addressed in future research are briefly given below:

(i) Include more realistic external circuits. This might take the form of transmission lines having frequency dependent impedances.

(ii) Evaluate the internal heating problem as a function of geometry and position. This might become important for analyzing the long-time behavior.

(iii) Extend the model to include antenna structures for directed electromagnetic energy radiation. Various types of antennas (i.e. spiral, horn, complementary etc.) could, in principle, be examined and studied.

(iv) The present model was based on a two dimensional (2D) model. The fields were taken to depend only on the in-plane x- and y-coordinates. As an enhancement, this code could be extended to the third z-dimension. While the implementation is expected to be very straight-forward, the computation times might become quite excessive.

(v) Other areas of future work might include a more in-depth analysis on a wider range of the operating parameters such as the operating temperature, the applied bias, the device dimension, and the pump laser wavelength.

REFERENCES

[1] For example, S. Maas, Microwave Mixers (Artech House Publishers, Boston, 1993).

[2] A. A. Saleh, Theory of Resistive Mixers (MIT Press, Cambridge, 1971).

[3] S. M. Sze, Physics of Semiconductor Devices (J. Wiley, N. York, 1981).

[4] D. V. Plant, D. C. Scott, D. C. Ni, and H. Fetterman, IEEE Microwave Guided Wave Lett. 1, 132 (1991).

[5] X. C. Zhang, B. Hu, J. T. Darrow, and D. H. Auston, Appl. Phys. Lett. 56, 1011 (1990).

[6] I. Brener, P. C. Planken, M. Nuss, M. Luo, S. Chaung, L. Pfeiffer, D. E. Leaird, A. M. Weiner, J. Opt. Soc. Am. B 11, 2457 (1994).

[7] M. Li, F. G. Sun, G. A. Wagonar, M. Alexander, and X. Zhang, Appl. Phys. Lett. 67, 25 (1995).

[8] M. Exter and D. Grischkowsky, Appl. Phys. Lett. 56, 1695 (1990).

[9] F. W. Smith, H. Lee, V. Diadiuk, M. A. Hollis, A. R. Calawa, S. Gupta, M. Frenkel, D. R. Dykaar, G. Mourou, and T. Hsiang, Appl. Phys. Lett. 54, 890 (1989).

[10] K. A. McIntosh, K. B. Nichols, S. Verghese, and E. R. Brown, Appl. Phys. Lett. 70, 354 (1997).

[11] J. F. Whitaker, Mater. Sci. Eng. B 22, 61 (1993).

[12] M. Klingenstein, J. Kuhl, R. Notzel, K. Ploog, J. Rosenzweig, C. Moglestue, A. Hulsmann, Jo. Schneider, and K. Kohler, Appl. Phys. Lett. 60, 627 (1992).

[13] Bahaa E. A. Saleh and Malvin Carl Teich, Fundamentals of Photonics (Toronto: John Wiley & Sons Inc., 1994), 907-909.

[14] T. W. Crowe, Intl. J. Infrared Millimeter Waves 10, 765 (1989).

[15] C. Rauscher, L. Goldberg, and A. M. Yurek, Electr. Lett. 22, 705 (1986).

[16] M. Ito and O. Wada, IEEE J. Quant. Electr. QE-22, 1073 (1986).

[17] E. R. Brown, J. R. Soderstrom, C. Parker, L. J. Mahoney, K. Molvar, and T. C. McGill, Appl. Phys. Lett. 58, 2291 (1991).

[18] F. Zernike and J. E. Midwinter, Applied Nonlinear Optics (Wiley, N. York, 1973).

[19] K. Victor, H. G. Roskos, and C. Waschke, J. Opt. Soc. Am. B **11**, 2470 (1994).

[20] H. Roskos, M. C. Nuss, J. Shah, K. Leo, D. A. B. Miller, A. M. Fox, S. Schmitt-Rink, and K. Kohler, Phys. Rev. Lett. 68, 2216 (1992).

[21] G. Rebeiz, Proc. IEEE 80, 1748 (1992).

[22] K. A. McIntosh, E. R. Brown, K. Nichols, O. B. McMahon, W. F. DiNatale, and T. M. Lyszczarz, Appl. Phys. Lett. 69, 3632 (1996).

[23] E. R. Brown, K. A. McIntosh, K. Nichols, C. L. Dennis, Appl. Phys. Lett. 66, 285 (1995).

[24] S. Y. Chou, Y. Liu, and P. B. Fischer, Appl. Phys. Lett. 61, 477 (1992).

[25] E. R. Brown, K. A. McIntosh, F. W. Smith, M. Manfra, and C. L. Dennis, Appl. Phys. Lett. 62, 1206 (1993).

[26] E. R. Brown, K. A. McIntosh, F. W. Smith, K. Nichols, M. Manfra, C. L. Dennis, and J. Mattia, Appl. Phys. Lett. 64, 3313 (1994).

[27] K. A. McIntosh, E. R. Brown, K. Nichols, O. B. McMahon, W. F. DiNatale, and T. M. Lyszczarz, Appl. Phys. Lett. 67, 3844 (1995).

[28] E. R. Brown, F. W. Smith, and K. A. McIntosh, J. Appl. Phys. 73, 1480 (1993).

[29] R. P. Joshi and J. McAdoo, Appl. Phys. Lett. 68, 1972 (1996).

[30] C. Moglestue, J. Rosenzweig, J. Kuhl, M. Klingenstein, M. Lambsdorff, A. Axmann, Jo. Schneider, and A. Hulsmann, J. Appl. Phys. 70, 2435 (1991).

[31] R. E. Lipsey, S. Jones, J. R. Jones, T. W. Crowe, L. F. Harvath, U. Bhapkar, and R. J. Mattauch, IEEE Trans. Electron Devices ED-44, 1843 (1997).

[32] R. H. Pantell, M. DiDomenico, O. Svelto, and J. N. Weaver, Proceedings of the Third International Conference on Quantum Electronics, edited by P. Grivet and N. Bloembergen (Columbia Univ. Press, N. York, 1964), Vol. 2, p. 1811.

[33] S. M. El-Ghazaly, R. P. Joshi, and R. O. Grondin, IEEE Trans. Microwave Theory Tech. MTT 38, 629 (1990).

[34] S. Tiwari, Compound Semiconductor Devices (New York: Academic Press, 1992).

[35] M. Kurata, Numerical Analysis of Semiconductor Devices (D. C. Heath, MA, 1985).

[36] C. Jacobani and P. Lugli, The Monte Carlo Method for Semiconductor Device Simulation (Wien: Springer-Verlag, 1989).

[37] C. Jacoboni and L. Reggiani, Reviews of Modern Physics 55, 645 (1983).

[38] H.D. Rees, Phys. Chem. Solids 30, 643 (1969).

[39] Michael Shur, Physics of Semiconductor Devices (Prentice-Hall Inc., New Jersey, 1990).

[40] J. B. Gunn, Solid State Comm. 1, 88 (1963); J. B. Gunn, IBM J. Res. Dev. 8, 141 (1964).

[41] Xiaolei Zhang and Kenneth K. Mei, IEEE Transaction on Microwave Theory and Techniques 36, 1775 (1988).

[42] K. S. Yee, IEEE Trans. Antennas Propag. 14, 302 (1966).

[43] D. Merewether, IEEE Trans. Electromagn. Compat. 13, 41 (1971).

[44] R. Holland and J. W. Williams, IEEE Trans. Nucl. Sci. 30, 4583 (1983).

[45] B. Engquist and A. Majda, Math. Comput. 31, 629 (1977).

[46] Jean-Pierre Berenger, J. of Computational Physics 114, 185 (1994).

APPENDIX A

BAND STRUCTURE OF GAAS

This appendix gives the basic knowledge about the GaAs band structure, which was applied many times in this thesis. All the information and figures of this appendix are cited from Chapter 1, Reference[39].

GaAs is a kind of covalent semiconductor material and its band structure is shown below in Figure A.1. We can see that the band structure of GaAs consists of one conduction band and three valence bands(heavy hole band, light hole band and split-off band). Inside the conduction band, there are three valleys called L valley, Γ valley, and X valley, respectively.

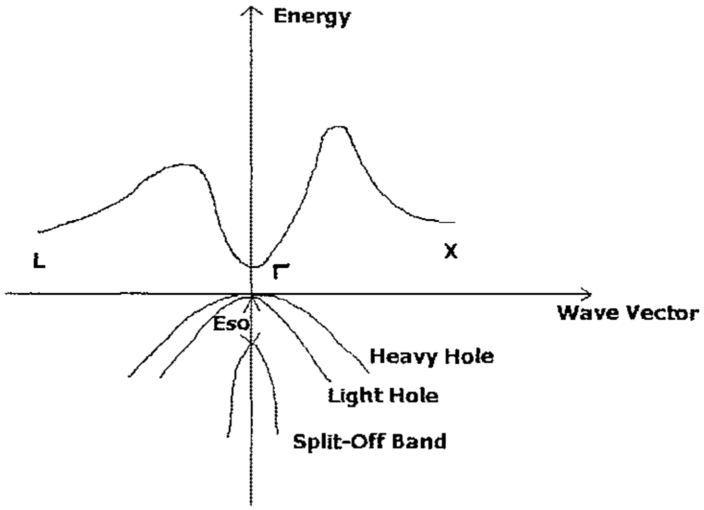

Figure A.1 Band structure of GaAs.

(Taken from Figure 1-5-6, Reference[39])

The tops of all theses three valence bands are located at the same point Γ. Among them, the light hole band and heavy hole band have the same energy at this point, while the split-off band is split by an energy of “Eso”. The lowest minimum of the conduction band is located within the Γ valley at the Γ point (k=(0,0,0)). The lowest minimum of the L valley is located at L point ($k = (\pi / a_0, \pi / a_0, \pi / a_0)$), while the minima of X valley is located along the Δ lines ($k = (\pi / a_0, 0, 0)$).

Near the bottom of the conduction band, or the top of the valence band, the carrier energy is a quadratic function of the momentum. And the following equations show different function forms for Γ, L, and X valleys:

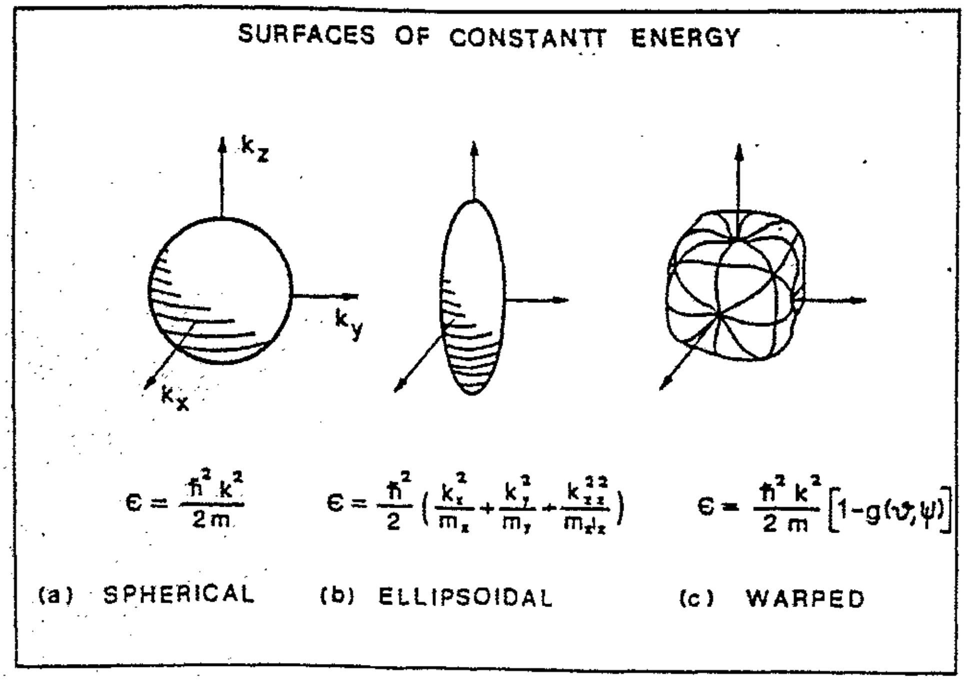

Figure A.2 Surface of constant energy.

(Taken from Figure 1-5-8, Reference[39])

$$E(k) = \frac{\eta^2 k^2}{2m}$$

$$E(k) = \frac{\eta^2}{2}\left(\frac{k_x^2}{m_x} + \frac{k_y^2}{m_y} + \frac{k_z^2}{m_z}\right)$$

$$E(k) = ak^2[1 \mu\, g(\vartheta, \psi)]$$

Figure A.2 draws the surfaces of constant energy for carriers at each valley. From this figure, we can see that the Γ valley has only one scalar effective mass, so its constant energy surface is spherical. L valley has a tensor effective mass, therefore has an ellipsoidal equivalent energy surface. For X valley, the equivalent energy surface is wrapped. And this shape is also appropriate to describe the heavy and light hole bands.

APPENDIX B

SCATTERING MECHANISM

This appendix gives the basic idea about various scattering mechanisms in the semiconductor, which is applied in this thesis. All the information, figures and equations are cited from chapter 12, Reference [39].

B.1 General Theory

The scattering mechanism in semiconductor can be classified into two parts: intervalley scattering mechanism and intravalley scattering mechanism. In the first case, both the initial and final states of the carriers are in the same valley.

B.2 Polar Optical Phonon Scattering

Polar optical phonon means two oppositely charged unit cells oscillate out of phase. Because of this, a polarization field is generated which scatters the electron. The scattering rate can be described as:

$$P(E) = \frac{2\sqrt{m^*}\,\omega_0}{4\sqrt{2}\pi\varepsilon_0\eta}\left[\frac{1}{\varepsilon_\infty} - \frac{1}{\varepsilon_0}\right]\frac{1+2\alpha E'}{\sqrt{E(1+\alpha E)}}F_0(E,E') \times (N_0 + \frac{1}{2} \pm \frac{1}{2}).$$

Where $E' = E \pm \eta\omega$,

and $F_0(E,E') = \ln\left[\dfrac{\sqrt{E(1+\alpha E)} + \sqrt{E'(1+\alpha E')}}{\sqrt{E(1+\alpha E)} - \sqrt{E'(1+\alpha E')}}\right].$

B.3 Non Polar Optical Phonon Scattering

In this mechanism, a shift in the electronic band state is generated by the non-polar optical phonons. So the carriers is scattered by this potential deformation with the rate given as:

$$P(E)=\frac{D_0^2(m^*)^{3/2}}{\sqrt{2}\pi\eta^2\rho(\eta\omega_0)}\sqrt{E'(1+\alpha E')}(1+2\alpha E')(N_0+\frac{1}{2}\mu\frac{1}{2}).$$

Where $E'=E\pm\eta\omega$ and $N_0=1/[\exp(\eta\omega_0/kT)-1]$

B.4 Acoustic Scattering

In the high field condition of this simulation, acoustic phonon scattering is considered as an elastic one because the energy change is very small compared to the carrier energy. But at low temperature, it is inelastic. The scattering rates in this simulation work can be expressed as(elastic form)

$$P(E)=\frac{(2m^*)^{3/2}k_B TE^2}{2\pi\rho s^2\eta^4}\sqrt{E(1+\alpha E)}(1+2\alpha E).$$

B.5 Ionized Impurity Scattering

This scattering mechanism is caused by the screened Coulombic potential. It is a elastic process, so, it cannot control the transport process under an external field until it is accompanied by some dissipative scattering mechanisms.

This process is usually treated by two different formulations: one is the Conwell-Weisskopf formulation, and the other is called Brooks-Herring formulation. In this simulation, we take the second formulation:

$$P(E)=\frac{N_I}{32\sqrt{2}\pi m}(\frac{Ze^2}{\varepsilon})^2\frac{1}{[\varepsilon_\beta/4\gamma(E)][1+\varepsilon_\beta/4\gamma(E)]}\frac{1+2\alpha E}{\gamma(E)^{3/2}}.$$

Where $\varepsilon_\beta=\eta^2\beta^2/2m$.

B.6 Intervalley Phonon Scattering

In this mechanism, a large amount of momentum transfer happens when carriers' states change between two different valleys. This large momentum is provided by an acoustic phonon or an optical phonon. This mechanism can be explained by the deformation potential concept and its rate is expressed as:

$$P_{ij} = \frac{z_j D_{ij}^2 (m_j^*)^{3/2}}{\sqrt{2}\pi\rho\eta^2 (\eta\omega_{ij})} \gamma_j^{1/2}(E^{'})(1+2\alpha_j E^{'})(N_{ij} + \frac{1}{2} \mu \frac{1}{2})$$

Where $E^{'} = E_j \ \mu \ \Delta_{ij} \ \mu \ \eta\omega_{ij}$

VITA

Jing Li was born in Wuhan city, P.R.China in In September 1991. He began his undergraduate study in Tsinghua University, Beijing, P.R.China. And he got his bachelor of engineering degree in the major of Electronic Engineering in June 1996. In January 1997, he began his graduate study at the Electrical and Computer Engineering Department in Old Dominion University, Norfolk, Virginia. He was a graduate assistant for Dr. Ravindra P. Joshi from January 1997 to December 1997.